Original Research Paper

IJES *Iranian Journal of Earth Sciences*
Vol. 16, No. 1, 2024, 13-39.
DOI: 10.57647/j.ijes.2024.1601.02

Fractal analyses of fracture network geometry: an example from the Tassili-n-Ajjers area, SE Algeria

Réda Samy Zazoun*

Sonatrach, Petroleum Engineering and Development Division, 8 Chemin du Réservoir, Hydra Algiers, 16035, Algeria

Received: 18 January 2023; Revised: 9 March 2023; Accepted 10 May 2023

Abstract

The objective of our study is to analyze the geometry of 2D fracture networks using fractal analysis methods. Three types of analyzes reflecting fractal behaviors, namely monofractal analysis, multifractal analysis and fractal anisotropy analysis are introduced as typical procedures to examine the density, the heterogeneity or the homogeneity, and the spatial-temporal directional relationship between the stress tensor and the fracture pattern generated by the fracture model, respectively. Further, a lacunarity dimension for describing the degree of self-organization is presented. An aerial photographic data set was used to extract fracture network lineaments from the Tassili-n-Ajjers area, Algeria. The scaling and distribution rules that characterize the spatial distribution of fractures were established using classical distribution laws and then revised in the light of Weibull distribution theory. The syn-fault fractures increase in frequency near the faults and we interpret the high fracture densities as a damage zones. The study reveals that multifractal and lacunarity data provides a more comprehensive understanding of the spatial heterogeneity of fracture networks than any monofractal dimension.

Keywords: *Algeria, Tassili-n-Ajjers, Fracture network, Fractal analyses, Weibull distribution*

1. Introduction

This paper investigates the methods involve analyzing the geometry of 2D fracture networks in order to represent fractured media. The quantitative analysis is centered on finding a mathematical rule that governs the geometry of fractured networks. We demonstrate how the use of a linear recognition, based on aerial photographs interpretation, and the fractal analyses, can make it possible to establish scale rules characterizing the fracture spatial distributions. The fractal principles can be applied to fracture networks to predict a generic fracture relationship at all scales. In geosciences, monofractal, multifractal and fractal anisotropy approaches are widely used to provide valuable knowledge on the statistical and geometrical properties of geological parameters (Table. 1)

According to Mandelbrot (1982), the concept of self-similarity is used to describe objects in which parts of them appear to be statistically similar to the entire object (Feder 1988). The power law distributions govern self-similarity and their exponents define the fractal dimensions (Odling et al. 1999). Several authors invoke the power-law distributions as fractal distribution, and in contrast to mathematical fractals, geological phenomena exhibit fractal behaviour within a limited scales range (Table 2). Bonnet et al. (2001) discussed 87 published fractal dimensions obtained from two-dimensional analyses, which vary from 1 to 2, the most frequent values clustering around 1.5 and 2.0. Values equal or very close to 2 probably correspond to non-fractal objects.

---

*Corresponding author.
E-mail address (es): reda-samy.zazoun@sonatrach.dz

However, power-law does not imply fractality (Bour and Davy 1997; Bour et al. 2002), and a general characterization should include geometrical parameters such as fracture density, lengths distributions, orientations, roughness of the surface failure, widths, openings and fault displacement (Bonnet et al. 2001; Zazoun 2008). In addition, various factors such as strength, tectonic history and lithology control the fractal dimension of a fractured rock mass (Tran et al. 2006 and Manjusha and Mukherjee (submitted) for other aspects of network of brittle planes (Mukherjee 2019).

This paper investigates the fractal geometry of the spatial fracture distribution in Tassili-n-Ajjers area. In order to reach this goal. Accordingly, we have:

1) mapped the fracture network from lineament interpretation of aerial photographic data set at scale of 1/80,000 ; (2) established the fracture density analysis (FDA); (3) studied the fault zones width (FZW); (4) analyzed the fracture length distribution (FLD); (5) examined the fractures topology (FT) and analyzed the fracture connectivity distribution (FCD); (6) analysed the fractures spacing (FSA); (7) measured the monofractal (mFA) and the multifractal (MFA) dimensions of the fracture map using the box-counting method (BCM) ; (8) We have also studied the fractal anisotropy analysis (FAA), lacuranity and (9) and used Weibull theory to describe fracture nucleation and growth.

The questions highlighted is: are there any auto-similar properties for the analyzed fracture network in the Tassili-n-Ajjers area?.

Table 1. Compilation of fractal studies for fracture systems

Authors	Field of investigation
Allègre et al. 1982	Scaling rules in rock fracture and possible implications for earthquake prediction
Barton and Larsen 1985	Fractal geometry of two-dimensional fracture networks
Chilès 1988	Fractal and geostatistical methods
La Pointe 1988	Fracture density characterization and connectivity through fractal geometry.
Vignes-Adler et al. 1991	Fractal analysis of fracturing from satellite imagery to ground scale
Turcotte 1992	Principles of fractals, chaos, and aspects of dynamical systems in the context of geological and geophysical problems
Cowie et al. 1993	Statistical physics model for spatiotemporal evolution of faults
Bour and Davy 1992	Clustering and size distributions of fault patterns (e.g. San Andreas fault)
Agterberg et al. 1996	Multifractal modeling of fractures (Lac du Bonnet batholith, Manitoba)
Ouillon et al. 1996	Hierarchical geometry of faulting
Giaquinta et al. 1999	The fractal properties of geological fault systems (Ethiopan Rift)
Bonnet et al. 2001	Scaling of fracture systems in geological media
Bour et al. 2002	A statistical scaling model for fracture network geometry (Hornelen Basin, Norway)
Darcel et al. 2003a	Stereological rules inherent in fractal fracture networks
Park et al. 2010	The temporal and spatial evolution of the fracture network
De Souza and Rostirolla 2011	Estimation of fractal dimension and multifractal spectrum of fractures
Kruhl 2013	Fractal-geometry techniques in the quantification of complex rock structures (Inhomogeneity and anisotropy)

Table 2. Compilation of fractal dimensions for fracture systems (N.A.: Not available)

Authors	Size of the system	Fractal Exponent
Barton and Larsen 1985	200-300m²	1.12 /1.16
Aviles et al. 1987	~3x10³m	1.01
Okubo and Aki 1987	~15x10³m	1.12
Hirata 1989	~25x10³/70x10³/73x10³m	1.49/0.72/1.60
Davy et al. 1990	~23x10³m	1.3
Matsumoto et al. 1992	~7x10³m/5x10³m	1.05/1.42
Gauthier and Lake 1993	~100x10³m	2.20/2.44/2.53
Gillespie et al. 1993	~238x10³m	2
Agterberg et al. 1996	450m	1.98/1.93
Berkowitz and Hadad 1997	~3x10³m /4000x10³	1.52/1.92/1.32/1.77
Cello 1997	~15x10³	1.60
Bodin and Razack 1999	~50x10³m	1.56
Bour and Davy 1999	~250x10³	1.65
Ehlen 2000	N.A.	1.7
Roy et al. 2007	N.A.	1.56 to 1.79
Zazoun 2008	~32x10³m X 65x10³m	1.84/1.91/1.94
Alizadeh et al. 2010	N.A.	1.41/1.66
Djezzar et al. 2020	N.A.	1.57/1.71

2. Geological background

The study area (Fig 1) is located on the southeastern part of the Algerian Saharan platform usually called the Illizi Basin, between the Berkine Basin to the north and the Touareg shield to the south. It is situated between latitudes 25°00'N and 26°43'N and longitudes 8°00'E and 9°00'E. The area of interest (Fig 1b) covers the southern branch of the NE-SW trending Fadnoun fault (F1). Near the North Fadnoun area (Fig 1b), it is possible to observe *en echelon* folded structures of Upper Devonian to Carboniferous age. The folded pattern corroborates the hypothesis of a N040° compression event consistent with the Hercynian stress field (Fig 1a) (Haddoum et al. 2001; Zazoun 2001 and 2008). This tectonic event was the origin of many inverted faults, mainly oriented N-S, in Paleozoic rocks (Galeazzi et al. 2010; Zieliński 2011; Peron et al. 2018).

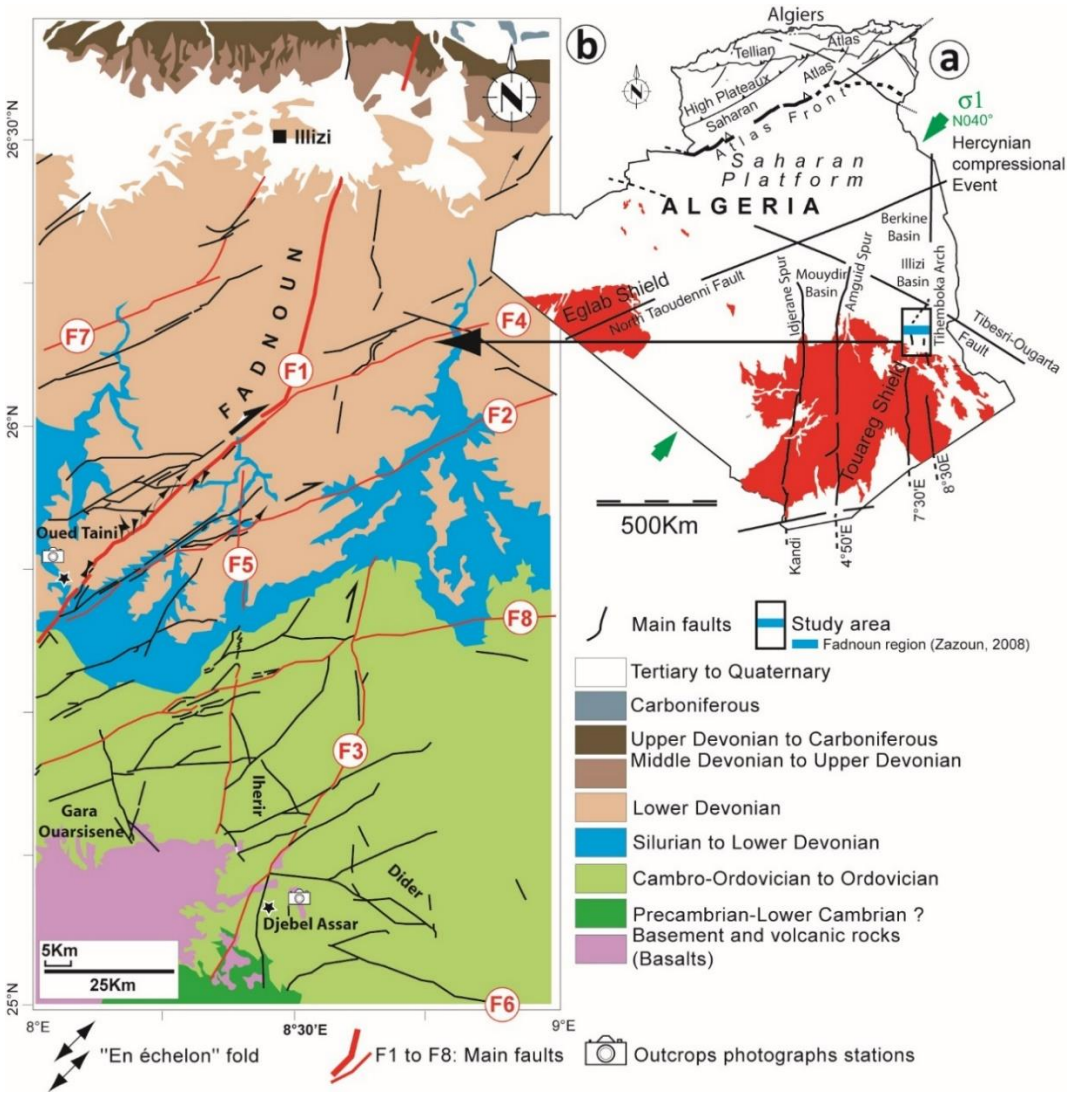

Fig 1. (a) Geographical setting of the studied area. The map shows the major structural features as well as the positions of the basins; Saharan platform main faults after Guiraud et al. (2000, 2005). (b) Geological setting of the Tassili-n-Ajjers area.

This paper does not include a detailed stratigraphic study. However, a lithostratigraphic succession is provided for comprehension purposes. (Fig 2). The Paleozoic sedimentary strata are entirely composed by siliciclastics, plus carbonates developed during the Carboniferous period. These are characteristics of a shield domain and stable tectonic conditions (Latrèche 1982; Fekirine and Abdallah 1998; Fabre 2005; Nosjean et al. 2020). The stable platform sedimentation during the Late Devonian continued into the Carboniferous with widespread deposition of fluvially-dominated deltaic sediments (Craig et al. 2008).

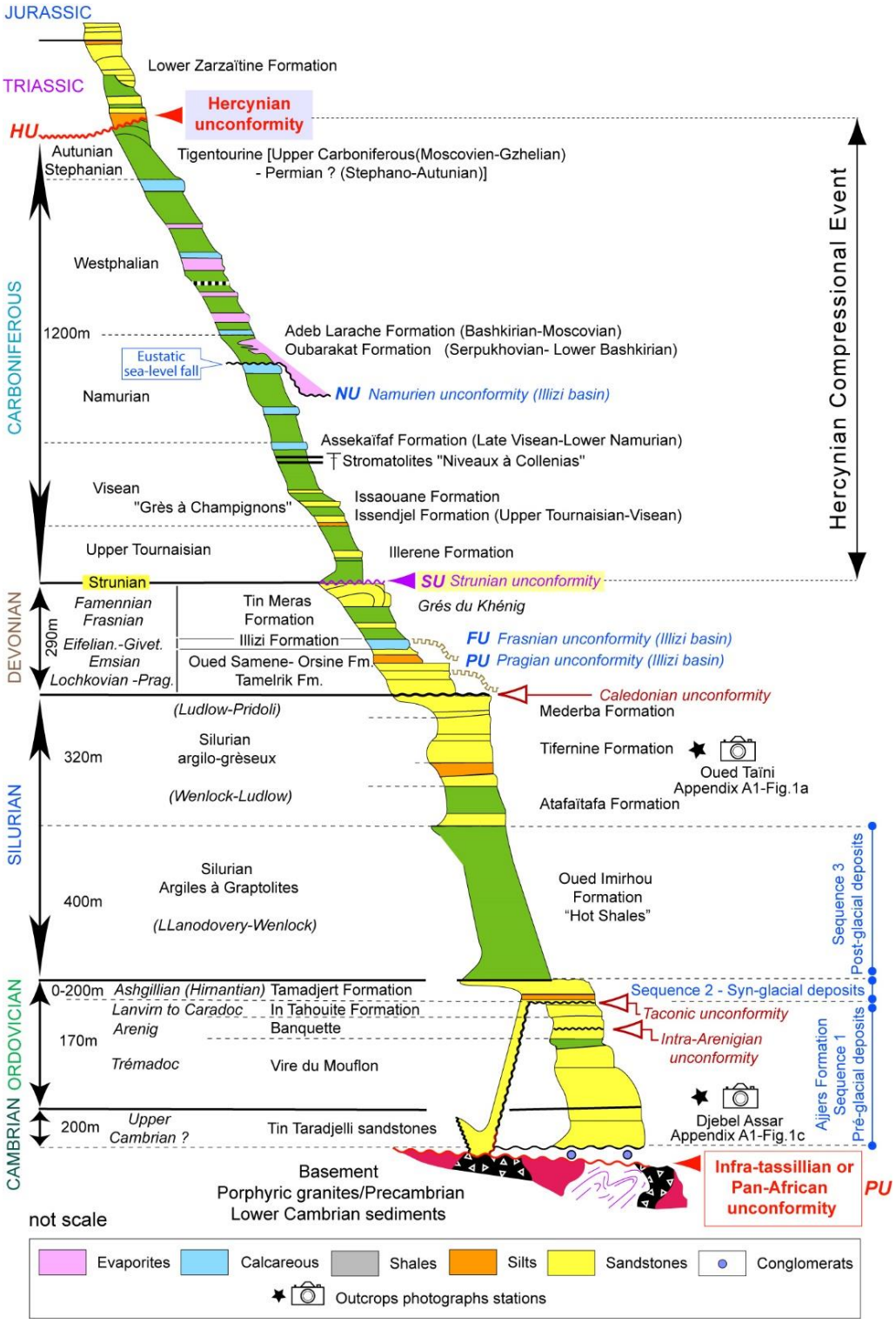

Fig 2. Lithostratigraphic succession of the Palæozoic formations of the Tassili-n-Ajjers area based on outcrop data (modified from Beuf et al. 1968 and 1971; Eschard et al. 2005; Fabre 2005).

(Taconic and Caledonian unconformities after Claracq et al. 1958; Late Ordovician glaciation period (Hirnantian) after Borroco and Nyssen 1959; Hercynian unconformity from Beuf et al. 1971; The first-order Lower Gondwana Cycle (Cambrian to Middle Devonian) corresponds to the second Arabian Plate tectono-stratigraphic megasequence of Sharland et al. (2001); the second-order sequences after Fekirine and Abdallah 1998).

3. Material and methods

2D lineament mapping was performed on aerial photos at 1:80,000 scale, covering an area of about 19602 km². This technique is used most often to highlight intense fracturing, tabular structure, and sub-vertical fractures (Fig 3). Effectively, the photogeology interpretation enables a suitable quantitative approach to fracture study. The fracture trace maps files were created in two (2) pre-process stages:

a- We imported digital aerial photos into Adobe Illustrator™ software and drew fractures traces, which are underlined as 'line' or 'polyline' elements.

b- The layer is saved with the fracture traces as an Encapsulated PostScript file (.EPS).

In total 2968 fractures were extracted from aerial photos (Fig 3); the minimum length was 29.12m, the maximum length was 98838.49m, with a mean length of 1483.66m. Using JMicroVision V1.2.7 Software (Roduit 2010), the extracted fracture was decomposed to the vertexes and pixels, and interpolation of this point produced the fracture density map by using the software Surfer Version 7.05. Golden Software, Inc. (1993–2001). The fracture trace start and the end point data, barycentre, length and orientation were exported to an Excel datasheet, and the rose diagram, graphs, and histograms were created. In this study, we designate all the discontinuities under the term of fracture, which refers to a representation of discontinuities on a 2D map.

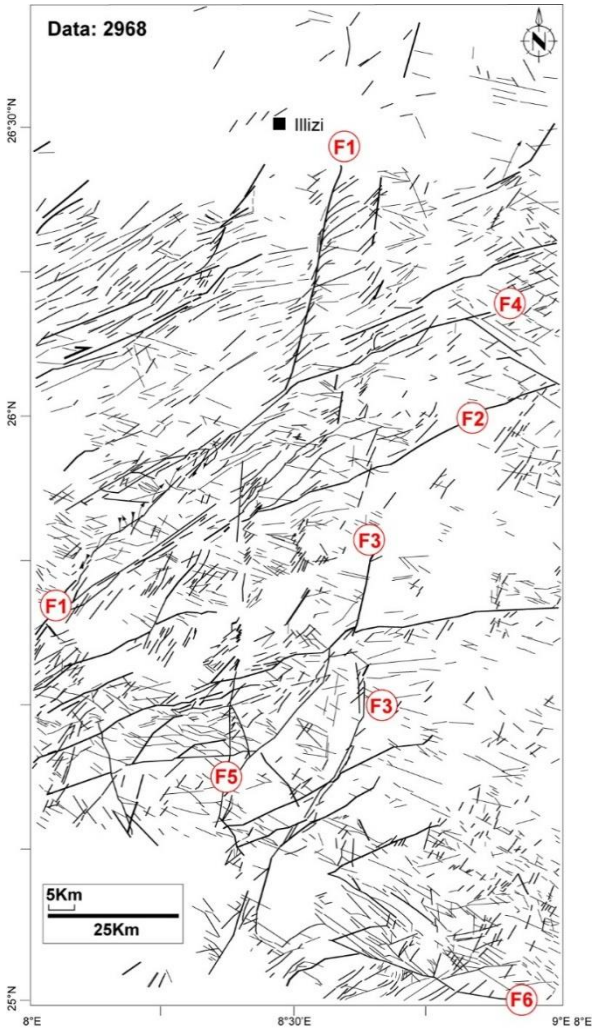

Fig 3. Map of fracture network of study area generated after the analysis of aerial photographs.

For the monofractal (mFA) and multi-fractal (MFA) analyses, FracLac Software (Version 2.0f ©, for Image J 1.40g) (Rasband 1997; Karperien 2004) was used to perform the box dimension method (BCM) (Allègre et al. 1982; Berkowitz and Hadad 1997; La Pointe 1988; Odling 1992). The box-counting method (BCM) (see Appendix A1. Fig 2b) (Chilès 1988; Tanaka et al. 1999; La Pointe 1988; Roy et al. 2007) is a suitable method for analyzing complex and isotropic 2D patterns, simple and non-centered (Kruhl 2013). However, this method is strongly affected by finite size effects (Afshari Moein et al. 2019) and it is sensitive to a change in fractal

dimension with scale (Blenkinsop 1994; Blenkinsop and Sanderson 1999). Hobbs et al. (2022) demonstrates that the box-counting method (BCM) for a spatial distributions of points is a method for calculating the nearest neighbour distribution (Carpena and Coronado 2019) which is a Weibull distribution (Weibull 1951) and not Pareto (see Appendix A2. Fig 1). it can sometimes seem to be a bifractal but such appearance has no physical significance. According to Mašín (2003), the Weibull distribution is extensively used in geological applications in the analysis of extreme value problems (Boadu and Long 1994; Lochmann et al. 2007) and it is successfully applied in many studies of the frequency-size distributions of fractures (Stoyan and Gloaguen 2011), dyke thickness (Krumbholz et al. 2014), rock fragmentation (Mašín 2003), fracture spacings (Boadu and Long, 1994) and seismic events analysis (Brandt 2019). The Weibull distribution analysis of the box-counting method (BCM) for the monofractal analysis and the geometrical parameters of fractures will be performed using the DEVELVE Software Version 4.13.0.0 (2000-2019) and Microsoft Excel (2016).

In order to estimate the box-counting dimension, the Euclidean space containing the pattern is divided into a grid of cells of size (ε) and those cells $N(\varepsilon)$ are counted which contain at least one fracture (Paredes and Elorza 1999). The process is repeated for a range of values of (ε).

On a double-logarithmic plot of $N(\varepsilon)$ and (ε), a fractal fracture pattern produces a straight line with slope -D*b* (Bonnet et al. 2001; Peternell and Kruhl 2009), such that (Eq. 1):

$$N(\varepsilon) \propto \varepsilon^{-D_b} \quad (1)$$

Where D*b* is the fractal dimension. For Euclidean objects, equation 1 defines their dimension, (e.g. 0<D*b*≤ 1 for a one dimensional object or 1<D*b*≤2 for a two dimensional object) (Mandelbrot 1982; Turcotte 1992; Gillespie et al. 1993)

The quantification of anisotropy is important in fracture networks because it controls directionality of fluid flow (Roy 2013). Several methods for determining the fractal anisotropy of structures in 2D have been developed. The analysis enables the construction of a fractal ellipse in which the directional data are fitted to an elliptical distribution (Volland and Kruhl 2004; Gerik and Kruhl 2009; Mamtani et al. 2012; Kruhl 2013). The method proposed is simple. It starts by making a morpho-lineaments map with aerial photos interpretation. The fractal set is then generated using Cantor's Dust Method (CDM) (see Appendix A1. Fig 2c) (Chilès 1988; Velde et al. 1990) and a compass-counting technique (CCT) (Volland and Kruhl 2004; Pérez-López et al. 2005; and Pérez-López and Paredes 2006). The fractal dimension of the spatial point distribution (*D0*) and the trend of the fracture profile on transect (δ) are obtained as parameters. The fracture profiles are taken with an increment of 2°, oriented clockwise from 0° to 360°, hence 180 transects are represented. Plotting these parameters (*D0*, δ) in a polar graph allows the determination of an ellipse, defined as the fractal ellipse of the lineaments' spatial distribution. Where the maximum fractal dimension (Dh*max*) is represented by the longest axis, while the shortest axis symbolizes the minimum fractal dimension (Dh*min*). Best-fit ellipses are drawn using a least-squares method (LSM) (Gander et al. 1995) performed by FindGraph, Version 2.49 software ©Uniphiz Lab Software. 2002-2016 (Vasilyev 2016). According to Pérez-López et al. (2005), the fractal ellipse presents a spatial–temporal directional relationship between the stress tensor and the fracture pattern generated. (Pérez-López and Paredes 2006).

It is recognized that the geometry of the fractures and the relationships between individual fractures or fracture sets play a crucial role in fluid flow properties. Regarding the interest of the fracture connectivity, the term topology refers to the spatial relationships between fracture planes. Manzocchi (2002) invoked the fracture connectivity ternary plot (Barton and Hsieh 1989; Barton et al. 1989), which uses the three vertices of a triangle to represent the I, Y, and X nodes (*nd*) in the fracture network (topological patterns). Nodes are labelled as 'I' (for isolated ends of traces), 'Y' (for branch points, splays, or abutments), or 'X' (for cross-cutting intersections) (Sanderson and Nixon 2015) (see Appendix A1. Fig 2d). After the patterns were normalised (Silva et al. 2021), a ternary diagram was created to help define the fracture connectivity. (Manzocchi 2002) showed that the connectivity can also be expressed in terms of a single parameter, *n* defined by Equation 1, Where, P_I = Proportion of I nodes, P_X = Proportion of X nodes, P_Y = Proportion of Y nodes, with $P_I + P_X + P_Y = 1$.

$$n = [4(1 - PI)/(1 - PX)] \quad (2)$$

The fracture datasets were analysed using the FracPaQ toolbox developed in MATLAB™ by (Healy et al. 2017), which aims to estimate fracture connectivity (see Appendix A1. Fig 2d) (Sanderson and Nixon 2005; Sanderson et al. 2019).

It is accepted in the literature, that a power law may be assumed to be a reasonable model for geometrical parameter (*p*) of fracture population (Davy et al. 1990; Davy 1993; Pickering et al. 1995; Bour and Davy 1997; Bour and Davy 1999; Odling et al. 1999; Lasm 2000; Bonnet et al. 2001; Darcel et al. 2003a; Hashemi and Baizidi 2018; Mansouri et al. 2020) when the distribution trend on a log-log graph shows an acceptable approximation to a straight line over a sufficient scale range. The geometrical parameter distribution of natural fractures obeys a power law distribution of size such that (eq. 3):

$$N(p) \propto p^{-a} \quad (3)$$

Generally, a given geometrical parameter of fracture populations is plotted as a normalised cumulative frequency distribution, Where N(*p*) is the number of fractures with (*p*) greater or equal to (*p*), and (*a)* is a

density constant. When bilogarithmic axes are used, a straight line indicates that the (p) distribution is power law with an exponent (a) given by the slope of the graph. Thus, the data used to generate the curve are limited at high values by the truncation artifact (resolution limitation) and at low values by the censoring artifact (incomplete sampling) which changes the distribution appearance. Consequently, only a portion of the curve, between (p min) and (p max) has a linear behavior and can be fitted with a power law expression: (Pickering et al. 1995; Odling et al. 1999; Bonnet et al. 2001; Ackermann et al. 2001; Zimmerman and Main 2004).

4. Results

4.1. Quantitative analysis of fracture data (QAFD)

The strike rose diagram, with an angular increment of 10° (Fig 4a), reveals that most of the fractures have a direction between N030°and N060°, with a cumulated percentage of 40.92% of fractures as a proportion and a weaker proportion in the N080°-120° direction (Fig 4b). Therefore, the fractures orientation is homogeneous and does show a two preferential fracturing direction. (N030°-N060° and N140°-N160°). As can be seen, the highest values of length (≥90000m) have a NE-SW (40°-60°) orientation with the proportion of 27.85%. 78 fractures were identified that have a length below 1000m with the weaker proportion of 3.37%. These fracture orientations are correlated with a Riedel system that defines bundles of fracturing. According to Zazoun (2008), the (40°-50) set, (80°-90) set, (50°-60°) set and the (20°-30°) set are interpreted, respectively as R (synthetic shear), R' (antithetic shear), Y and P of Riedel shears system (Tchalenko and Ambraseys 1970) compatible with the Hercynian shortening direction oriented N040° (Figs 1a and 4b) (Boudjema 1987; Haddoum et al. 2001; Zazoun 2001).

The log-log diagram of the cumulative fracture orientation frequency shown in Figure 4c attests that the fracture orientation distribution follows a logarithmic distribution function with correlation coefficient (R^2) of 0.91 (Table 3). (Eq. 4)

$$N(\geq Ot) = -983.1 * \ln(Ot) + 5427.6 \quad (4)$$

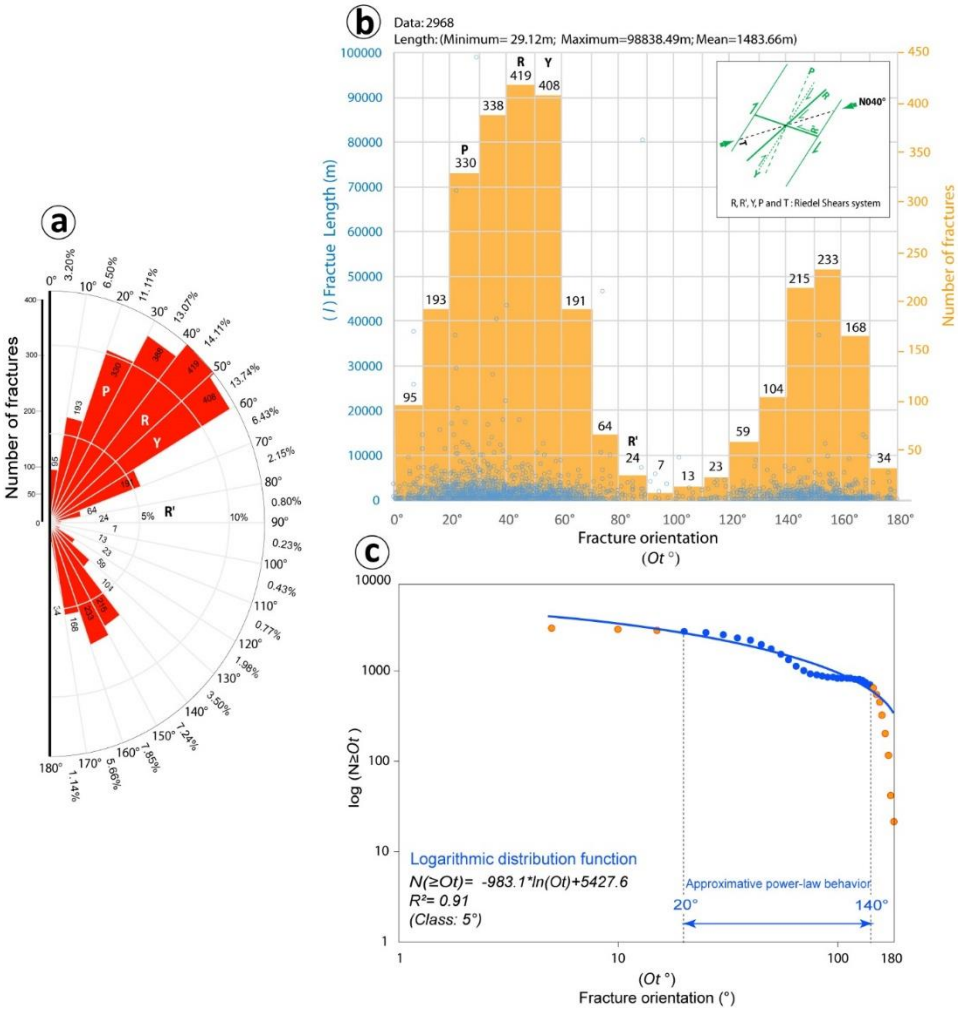

Fig 4. (a) Orientation diagram of the fracture network. (b) Fracture length (l) Vs. fracture orientation (Ot°) and fracture Number Vs. fracture orientation (Ot°). (c) Cumulative fracture orientation frequency distribution per 5° class orientation.

Table 3. Analyses results of cumulative frequency distribution of fractures parameters

	R^2	Class	Min.	Max.	Function
Quantitative analysis of fracture data (QAFD)	0.91	5°	0°	180°	Logarithmic
Fracture density analysis (FDA)	0.95	1 Frac./Km²	1 Frac./Km²	7 Frac./Km²	Exponential
Fault zones width (FZW)	0.22	0.29m	18.16m	988.32m	Logarithmic
Fracture length distribution (FLD)	0.96	7m	29.12	98838.49m	Logarithmic
Fracture connectivity distribution (FCD)	0.99	1 node	1 nodes	11 nodes	Exponential
Fracture spacing analysis (FSA)	0.79	1m	7.23	137.86	Exponential

4.2. Fracture density analysis (FDA)

One of the most important fracture-related parameters is the fracture density or the number of fractures per unit area (P20 of Dershowitz and Einstein 1988), which have been studied by several authors (Zazoun 2008; Zazoun et al. 2015; Andrews et al. 2019; Hashemi and Baizidi 2018; Mansouri et al. 2020). According to the fracture density map (*d*) (Fig 5a), seven relative fracture density classes were produced along with contour line generation. Color is blue for the lowest fracture density and red for the highest fracture concentration. Based on this map, the strong values of isofracturing (≥5 fractures / Km²) are localised along the main faults F1, F4, F5 and F6. The maximum value of density (7 fractures/Km²) observed in the region belongs to the Fadnoun and the Dider areas.

Figure 5b shows a log-log diagram of cumulative fault density distribution data per 1 fractures/Km² for the FDA class. The resulting distribution function is close to an exponential function (correlation coefficient R^2= 1) (Table 3).

$$N(\geq d) = 8.49\mathrm{E}^{+3} * e^{-0.98*d} \quad (5)$$

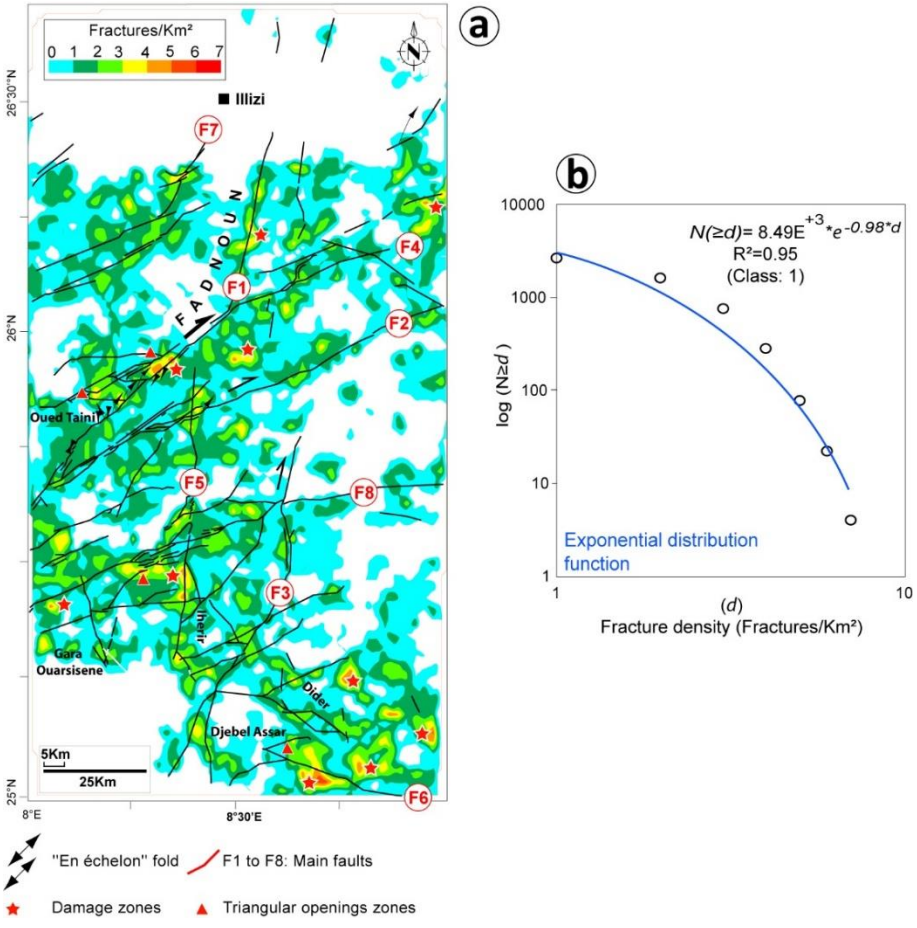

Fig 5. (a) Isodensity fracture map of the study area. Note the damage zones are localised along the main faults. (b) Cumulative fracture density frequency distribution.

To better understand the relation between fractures and faults, we established the graphs of cumulative number of fractures versus the fault positions along four scanlines oriented perpendicular to the dominant fracture strike (Fig 6). The graphs show a clear increase of the fractures number near the main faults (F1 to F8). (Peacock 2001) showing that the syn-fault fractures tend to increase greatly in frequency near the fault. It is commonly assumed that fracture frequency or network complexity increases close to the faults and in damage zones around them (Fig 6) (Wheeler and Dixon 1980; Pohn 1981; Hanks et al. 1997; Peacock 2001; Kim et al. 2004; Zazoun 2008).

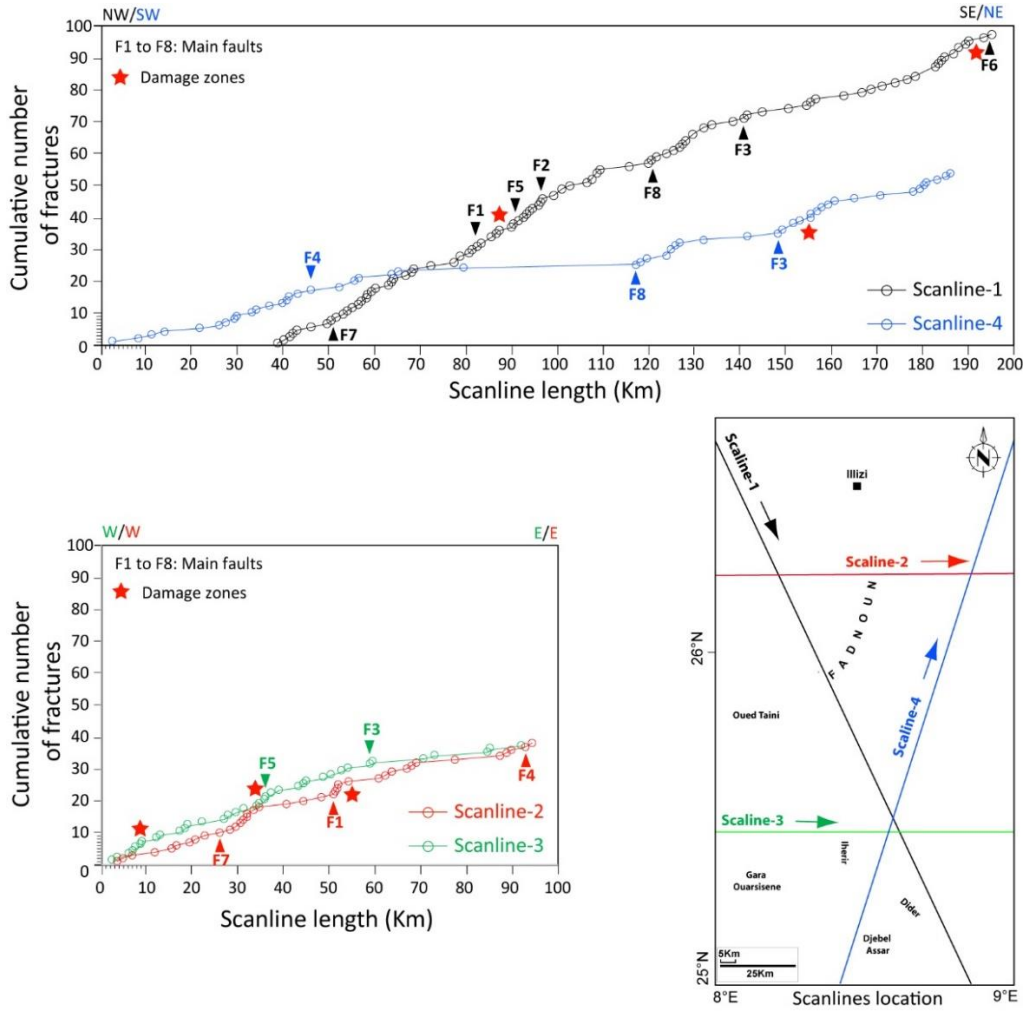

Fig 6. Graphs of cumulative number against distance along scanline length. Note the evidence of an increase in fracturing near the main faults (F1 to F8).

4.3. Fault zones width (FZW)

According to Choi et al. (2016), mature fault zones can be more complex due to the presence of anastomosing strands of fault gouge, lenses of damaged rock, and localised fault planes within damage zones (Fig 5a), and the fracture zones are surrounded by relatively undeformed host rock (Faulkner et al. 2003; Kim et al. 2004; Felici 2016; Choi et al. 2016; Delogkos et al. 2020). Scholz (2002) proposed an equation that relates the fault length to its width (Eq. 6), where Fzw=fault zone width, and L*f*=fault length.

$$Fzw = 0.01 \times Lf \quad (6)$$

The log-log diagram of fault zones width distribution data per 0.29 m width class confirms that the fault zones width distribution follows an exponential law function with a correlation coefficient (R^2) of 0.88 (Fig 7 and Table 3) (Eq. 7). In addition, it should be noted that the curve does not meet the strict exponential relationship within the fault zones width range. A dividing point is found at the fault zone with *Fzw*=4.35m; there is a scale-free interval on both sides, where the fitting formula is shown in figure 7.

$$N(\geq Fzw) = 27.72 * e^{-0.05*Fzw} \quad (7)$$

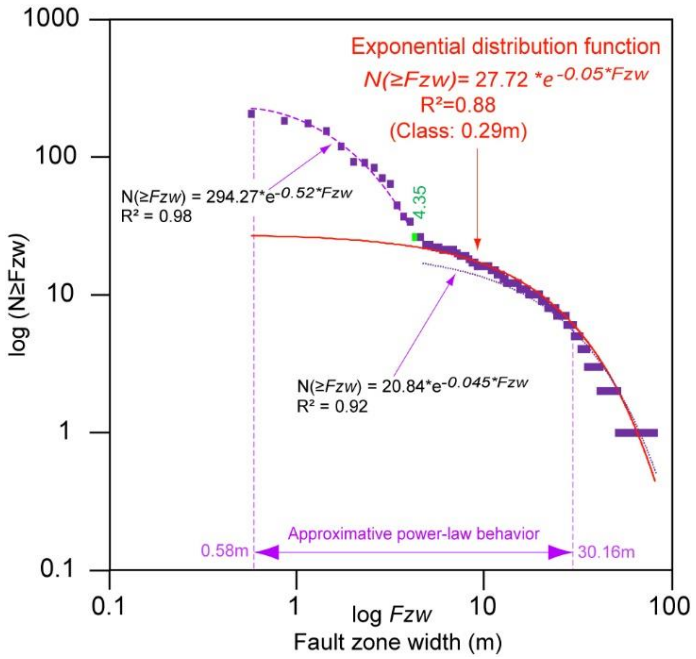

Fig 7. Cumulative fault zone width distribution of fracture network.

4.4. Fracture length distribution (FLD)

Size length distribution plays an important role because, for the same orientation distribution and density, collections of short fractures are less well connected than collections of long fractures (Balberg and Binenbaum 1983; Balberg et al. 1991). Bodin and Razack (1999). According to (Spyropoulos et al. 1999; Gupta and Scholz 2000; Ackermann et al. 2001), in the cumulative length distribution, the observed data at higher strains are best fit using an exponential relationship, whereas, at lower strains a power-law relationship provides a better fit (Hashemi and Baizidi 2018. Unfortunately, the log-log plot is often curved (Fig 8), suggesting that the power-law distribution is not a complete description of the fracture-trace lengths (Clark et al. 1999). The distribution would be much closer to a Weibull distribution (Fig 14).

Figure 8 shows the log-log diagram of cumulative length distribution data per 7m length class attests that the fracture length distribution follows a logarithmic distribution function with correlation coefficient (R^2) of 0.96 (Table 3). (Eq. 8)

$$N(\geq l) = -614.9 * \ln(l) + 5350.4 \quad (8)$$

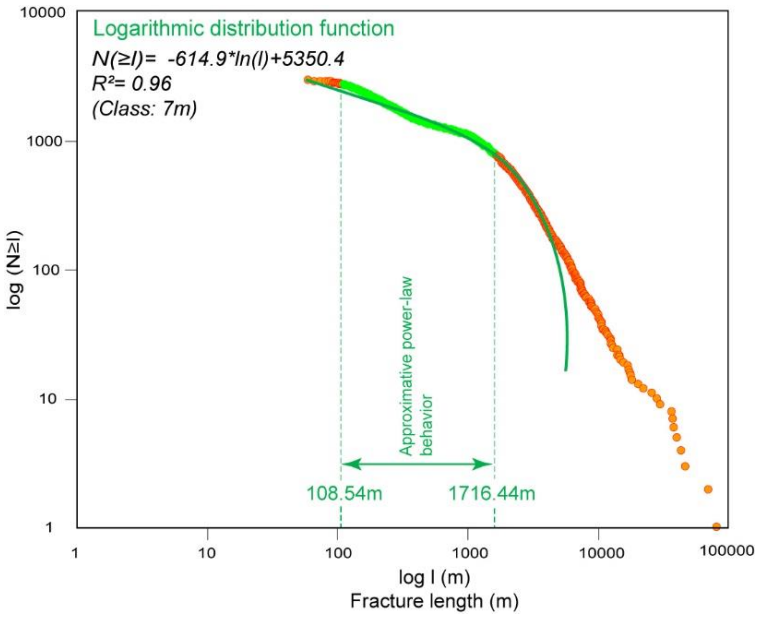

Fig 8. Cumulative fracture length frequency distribution.

4.5. Topology of fractures (FT) and the fracture connectivity distribution (FCD)

The fracture network in the area of study shows that 21% of fractures are slay, 36% have intersection with each other, and 43% of fractures are isolated. the connectivity is dominated by I and X nodes and the calculated parameter (*n*) in our case is equal to 3.56 (Fig 9a). The connectivity line (CL) in our case is greater than 2, and less than 3.57, which makes it possible to consider that the network fracture system is connected.

The log-log diagram of fracture connectivity distribution (FCD) data per 1 node (*nd*) class confirms that the node distribution follows an exponential function distribution with a high correlation coefficient (R^2) of 0.99 (Eq. 9) (Fig 9b and Table 3).

$$N(\geq nd) = 4.86\mathrm{E}^{+3} * e^{-0.66*nd} \quad (9)$$

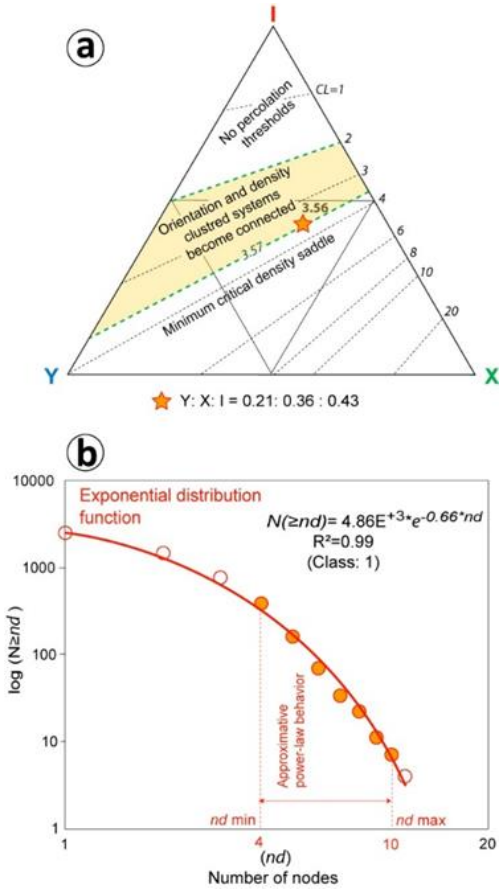

Fig 9. (a) Connectivity of fracture networks in the study area; the connectivity is dominated by I and X nodes. According to Sanderson and Nixon (2015), the dashed lines show specific numbers of intersections per line, with CL= 2 representing a limit above which a spanning cluster is not possible and CL =3.57 the value widely reported from random line simulations. (b) Cumulative fracture connectivity (I, X and Y nodes) frequency distribution per 1 node class.

4.6. Fracture spacing analysis (FSA)

For fracture spacing analysis, some authors have considered the totality of discontinuities (Hudson and Priest 1983; Baka et al. 2014); other authors make a selection based on orientation and/or type of discontinuities (Bouroz 1990). In our approach, the spacing is defined as the distance between two successive fractures along the sampling line without regard to the different sets (ie., orientations). In order to investigate the spacing law distribution. We proceeded to a representation of the cumulative fracture spacing frequency distribution in a log-log diagram (Gillespie et al. 1993) (Fig 10b) along scanlines oriented from the N to the E, with an increment of 10° (Fig 10a). The distribution of the cumulative spacing frequency obeys an exponential law distribution such that (Eq. 10) with a correlation coefficient (R^2) of 0.79 (Table 3):

$$N(\geq S) = 8.73\mathrm{E}^{+1} * e^{-0.02*S} \quad (10)$$

The sample statistical parameters (the mean, the median and the standard deviation) have been calculated (Fig 9b). A measure of the spatial distribution is given by the coefficient of variation *Cv* which is defined as the standard deviation divided by the mean spacing (Cox and Lewis 1966; Odling et al. 1999). According to Odling et al. (1999) and Ackermann et al. (2001), If the traces are regularly spaced the standard deviation of spacing is small and *Cv* < 1. If fractures are clustered, the standard deviation is large and *Cv* > 1. The coefficient of variation *Cv* calculated is equal to 5.67 (Fig 10b). therefore, higher than 1. The model defined by the scanline technique is confirmed by the coefficient of variation *Cv* which indicates a negative exponential distribution law (Fig 10c).

4.7. Fractal analyses

4.7.1. Monofractal analysis (mFA)

Several authors (Bonnet et al. 2001; Riley et al. 2011; Kruhl 2013) have used fractal analysis techniques to characterise the two-dimensional geometry of fracture networks since (Mandelbrot's 1967, 1982, 1985) work on the concepts of fractal geometry. In recent years, applications of monofractals (Velandia and Bermúdez 2018) and multifractals (Xie et al. 2010; Ord and Hobbs 2019) analysis have been increasing in the earth sciences. However, the fracture networks fractal dimension does not allow us to understand the state of fractures connectivity within the fractures network (Bonneau 2014). The 2D fracture networks in the Tassili-n-Ajjers have been the subject of a monofractal study by Zazoun (2008), however this study is restricted to the Fadnoun region (Fig 1a). A monofractal analysis (mFA) was undertaken on the structural map to determine the fracture spatial distribution. For the monofractal analysis (mFA), the fractal dimension (*Db*) was calculated for the structural map (Fig 11 and Table 4), and shows the dimension values obtained by box-counting method (BCM). the points can be fitted by an equation expressed as Equation 11. The global fracture network showed a monofractal dimension of D*b* = 1.56.

$$N(\varepsilon) = 4.9\varepsilon^{-1.56} \ (R^2=0.92) \quad (11)$$

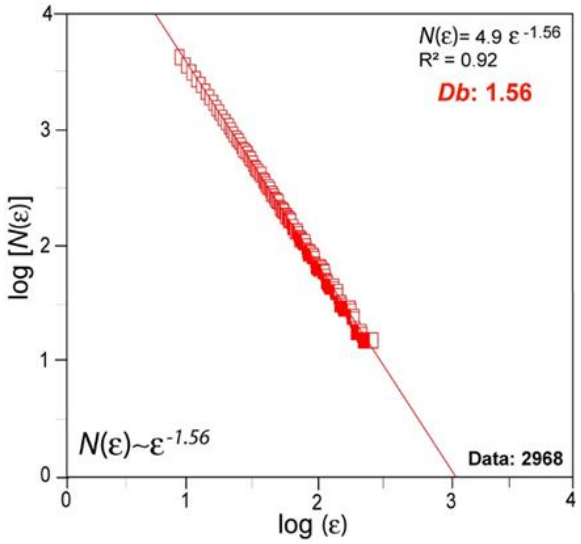

Fig 11. Monofractal analysis (mFA) of the fracture network using the box counting method (BCM). The fractures boxes can thus be taken as a fractal system with a dimension 1 ≤D*b*≤2.

4.7.2. Fractal anisotropy analysis (FAA)

The line fractal anisotropy analysis (FAA) results for the fractures map are shown in Figure 12, and are commented on below:

the maximum horizontal fractal dimension (Dh*max*= 0.89) is oriented N067°, with □= 23° and the minimum horizontal fractal dimension (Dh*min*= 0.74) is oriented N157° with (Azimuthal anisotropy of fractal dimension (AAD) =1.20 (Fig 12 and Table 4).

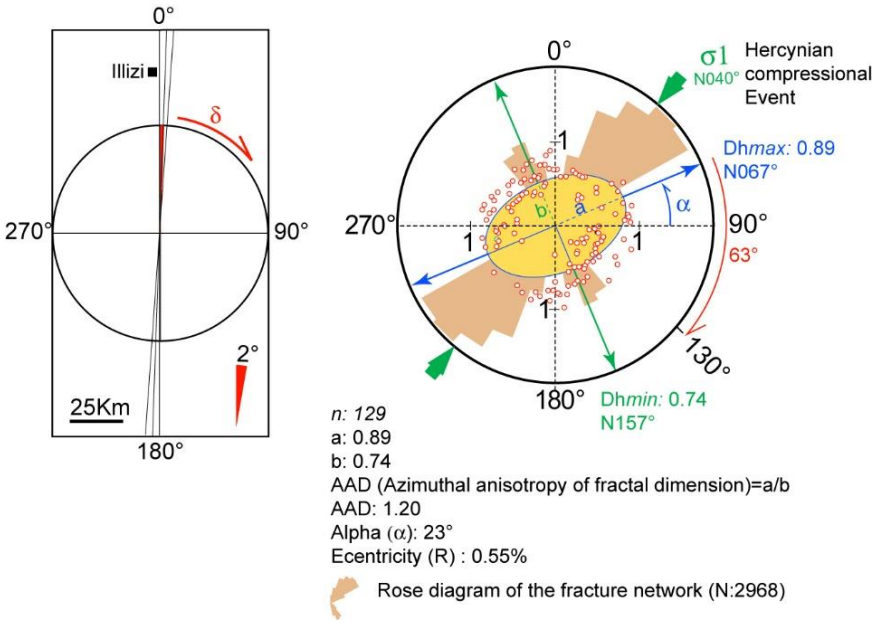

Fig 12**.** 1-Polar plot of 1-D fractal dimension, calculated by fractal anisotropy analysis (FAA).

4.7.3. Multifractal analysis (MFA)

According to Khider (2011), when we use several methods of calculating the fractal dimension, and we find very different results then this means that the object is very complex. The fractal dimension alone cannot fully characterize the complexity. He found it necessary to introduce the local fractal dimension to describe the roughness fluctuations at each point (Stoyan and Stoyan 1994). Indeed, when the fractal dimension changes from one point to another, we say that the fractal object is inhomogeneous or multifractal (Peitgen et al. 1992). Thus, the multifractal analysis (MFA) definition was developed to address requirements that the normal fractal (‘monofractal') approach could not address. Indeed, multifractal analyses can reveal more detail about spatial object measurements than monofractal

analyses. The standard partitioning approach within the moment-based multifractal model is the box-counting method (BCM), in which the studied space is partitioned into non-overlapping boxes (Hentschel and Procaccia 1983; Halsey et al. 1986; Evertsz and Mandelbrot 1992; Cheng 1999; Deng et al. 2011: Kruhl 2013). In the case of monofractal analysis, scaling is defined by only one exponent. While for MFA, a generalised dimensions *D(q)* and the multifractal spectra *f*(□) are used to describe the fractal characteristics (Turcotte 1992; Cao et al. 2017; Liu et al. 2021). According to Bonnet et al. (2001), the box-counting method (see Appendix A1. Fig 2b), which only characterises the scaling properties of the fracture network's spatial occupancy, is frequently supplemented by the scaling properties of the fracture densities via moments of order *(q)*. The system is first covered in a regular mesh of squares with side lengths (ε) and total length *Li*, and the probability *Pi* (ε) is defined as follows (Eq. 12):

$$P_i(\varepsilon) = L_i(\varepsilon) / \sum_1^n L_i(\varepsilon) \quad (12)$$

Where the sum is applied to all boxes and simply returns the total cumulative length of all fractures. After that, the moments of order *q* are then constructed (Eq. 13):

$$M_q(\varepsilon) = \sum_{i=1}^{n} P_i^q = \varepsilon^{\tau(q)} \quad (13)$$

The multifractal is confirmed when the slopes of fitting □(q) satisfies the power law relationship (Eq.14) for a range of values of q.

$$M_q(\varepsilon) \propto \varepsilon^{\tau q} \quad (14)$$

Where□□(q) is called the mass exponent of *q* order and the generalized fractal dimension is calculated as follows: (Eq. 15).

$$D(q) = \frac{1}{q-1} \lim_{r \to 0} \left(\frac{Mq(\varepsilon)}{\ln \varepsilon} \right) = ^n \frac{\tau(q)}{q-1,} \quad (15)$$

The multifractal spectra as a plot of f(α) against - α can be obtained as follows: (Eq. 16 and 17).

$$\alpha(q) = \frac{d\tau(q)}{dq} \quad (16)$$

$$f(\alpha) = q(\alpha)q - \tau(q) \quad (17)$$

where the α(q) is a singular exponent and a monotone decreasing function, which reflects the singularity intensity of fractures and represents the probability of fractures in the area of the study. The selection of appropriate box sizes and the range of moment orders is critical for multifractal analysis (MFA). We used a criterion based on evaluating the linear behaviour of the mass exponent *D(q)* as a function of *q* to find these ranges. Figure 13a shows plots of *D(q)* vs. *q* for various q values. The dimensions used are known as *q*=0 (the capacity or the fractal metric dimension), *q*=1 (the information dimension or the Shannon entropy) and *q*=2 (the correlation dimension) (Saucier and Muller 1999; Bonnet et al. 2001). According to Hentshel and Procaccia (1983), for the multifractal analysis (MFA), *D(q)* behaves predictably, decreasing as *q* increases. The procedure for calculating the multifractal spectra is carried out with *q* ranging from -10 to +10, in increments of 1. Korvin (1992) asserts that equality in these three dimensions occurs only when the geometry is monofractal or single fractal. The results of the multifractal analysis (MFA) indicate that the fracture intensity spatial distribution has a heterogeneous fractal structure, with generalized positive fractal dimensions. Indeed, the nonlinear slopes characteristic of the exponent *D(q)*, adjusted in the partition functions for each moment *q*, make it possible to ensure that there is multifractal behaviour in the analyzed two-dimensional fracture fields (Fig 3). As a result, *D(q)* follows a predictable pattern, non-decreasing as *q* increases: *(D0*=1.84>*D1*=1.81>*D2*=1.80>*D3*=1.79>*D4*=1.78>*D5*=1.77>*D6*=1.76>*D7*=1.75>*D8*=1.74>*D9*=1.7).

(Fig 13a and Table 4). For a monofractal, all the dimensions become similar to *D0*. The value of *D0=D1=D2* indicates that the distribution is homogeneous and exhibits perfect self-similarity. Nevertheless, for the multifractal analysis *D0>D1>D2* (Biswas et al. 2012). As shown in Figure 13b, a graph of multifractal spectra *f* (α) vs (α) reveals a multifractal behaviour. Indeed, if the graph is arched, the scaling is considered multifractal. Conversely, if the dimensions converge, the scaling is considered mono- or non-fractal (Kaperian, 2004). A quadratic equation fitting (*f* (*q*)=Aα²+Bα-C) was adjusted and calculated for the fitting curve, where the parameter (B) describes the symmetry of the fractal spectra. When B=0, then *f*(*q*) is symmetric, While, when B≠0, *f*(*q*) is asymmetric (Liu et al. 2021). In our study, the multifractal spectra *f* (α) appears as an asymmetrical parabola, and it reaches a maximum at α (*q*)=2.44, with B=15.06 (>0) and Δ*f*=0.51 (>0). The multifractal behavior should be confirmed by the convex shape of the τ (q) curve. The Figure 13c shows that the shape of the curve is not really convex. Even if the error bars on D*0*, D*1* and D*2* could not be calculated. It is highly likely that the behavior is monofractal.

Likewise, the minimum value of multifractal parameters (α*min*=1.67) corresponded to *q* = 9, and the maximum value (α*max*=2.61) corresponded to *q* = -8. The calculated value of Δα (αmax - αmin) and the asymmetrical index (AI) in our case, are respectively equal to 0.94 and -0.57 (Fig 13b and Table 4).

4.7.4. The lacunarity (Λ(ε))

The term lacunarity comes from the Latin word "Lacunas" which means hole or gap. According to Sahu et al. (2020), in the case of deterministic fractal fracture models, the fractal dimension is not a unique identifier of the properties of connectivity or flow. In fact, it is the fracture networks clustering that is used to understand connectivity, because there is a notable correlation between the connectivity and lacunarity parameter which quantifies scale-dependent clustering. The term lacunarity is a parameter that measures the degree of clustering at a given spatial resolution and characterizes the distribution of spaces or gaps in a pattern as a function of scale (Mandelbrot 1982; Plotnick et al. 1996). For both fixed box (overlapping or sliding) and

non-overlapping box counting method, lacunarity is determined from the probability distribution for pixels from the binary image of the fracture network. Its implementation is simple. It suffices to calculate the variance $\sigma^2(\varepsilon)$ and the mean $\mu(\varepsilon)$, in all non-zero pixel size boxes (ε), then to deduce the fractal lacunarity ($\Lambda(\varepsilon)$) given by the formula (Eq.18) (Plotnick et al. 1996).

$$\Lambda(\varepsilon) = \frac{\sigma^2(\varepsilon)}{(\mu(\varepsilon))^2} + 1 \quad (18)$$

This operation is repeated for each box size (ε) as many times as necessary to deduce all the values of the curve of the lacunarity ($\Lambda(\varepsilon)$).The calculated value of variance ($\sigma^2(\varepsilon)$) and the mean ($\mu(\varepsilon)$) for the global fracture network, range respectively $0.09 \leq \sigma^2(\varepsilon) \leq 651.21$ and $1.1 \leq \mu(\varepsilon) \leq 10.5$.

Figure 13d illustrates the linear relationship between the lacunarity index ($\Lambda(\varepsilon)$) and the box size (ε) in the bi-logarithmic plot. The data show that the lacunarity value ($\Lambda(\varepsilon)$) decreases from 6.90 to 1.07 as the value of the box size increases from 1km to 95km. That is, the lacunarity depends heavily on the size of the model (Allain and Cloitre 1991; Plotnick et al. 1993; Giri et al. 2016). The data can be fitted by a straight line only between, ε=1Km m and ε=56Km exhibiting multifractal behavior over that range. According to Marwan et al. (2007), this linear decrease reveals a large amount of self-similarity. However, for all data, the obtained values can be fitted using a linear function law with correlation coefficient (R^2) equal to 0.90. (Eq. 19), corresponding to a beta lacunarity exponent of -2.13.

$$\Lambda(\varepsilon) = 0.49(\varepsilon) + 0.86 \quad (19)$$

Table 4. Fractal analyses results. For the multifractal analysis (MFA), the Renyi dimensions (D0, D1, and D2) calculated are close in values, which indicates that the fractures network is probably monofractal.

	Monofractal analysis (mFA)	Multifractal Analysis (MFA)	Fractal anisotropy analysis (FAA)
Db	1.56	-	-
R^2	0.92	-	-
D0	-	1.84	-
D1	-	1.81	-
D2	-	1.80	-
D0-D1	-	0.03	-
D1/D0	-	0.98	-
Dh*min*	-	-	0.74 (N157°)
Dh*max*	-	-	0.89 (N067°)
AAD	-	-	1.20
Δα	-	0.94	-
ΔαL	-	0.20	-
ΔαR	-	0.74	-
AI	-	-0.57	-
Δ*f*	-	0.51	-

5. Weibull distribution of the geometrical parameters of fractures

The Weibull distribution is a continuous probability distribution and is one of the most popular distributions in analyzing skewed data (see Appendix A2. Fig 1). The reason to use a Weibull distribution is because of its flexibility, due to its different forms of probability density functions (PDF) and due to the monotonicity property of the hazard function. It has a closed form cumulative distribution function (CDF) and it can be used very effectively for analyzing censored data (Lai et al. 2006; Joarder et al. 2011).

The results of Weibull distribution of fractures parameters (Fig 14) are reported in table 5. From this table, it is evident that all the shape parameter (κ) calculated for each geometrical parameter is >1. So we can consider that Weibull analysis estimates that these parameters increase with time. According to Hobbs et al (2022), the physical significance of the Weibull probability distribution function (PDF) corresponds to systems that nucleate quickly, grow competitively and have short extinction times due to relatively strong competition (Lavenda 1995).

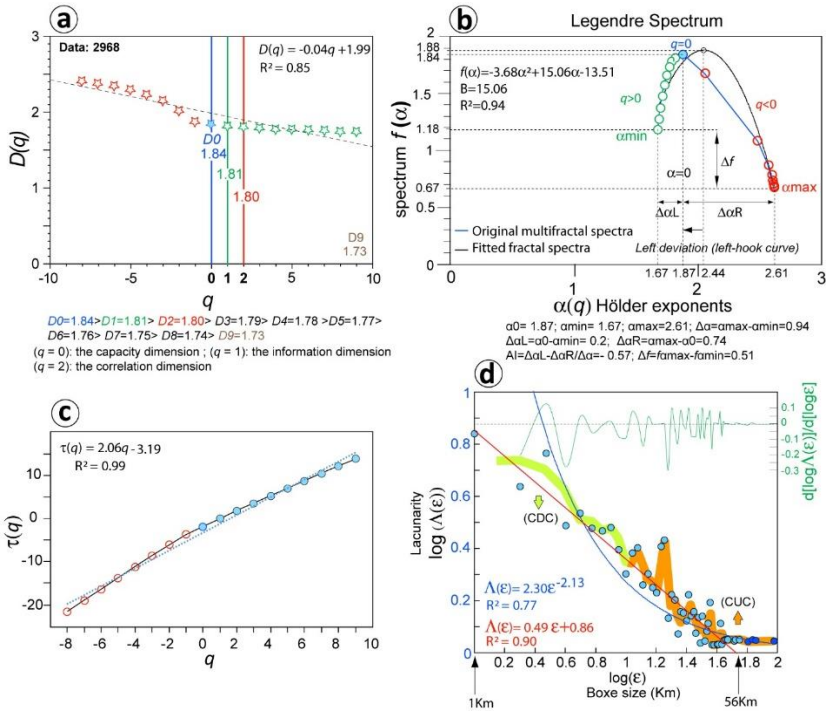

Fig 13. Multifractal analysis (MFA) of the fracture network: (a) Generalized dimension graph; *D0*=1.84, *D1*=1.81 and *D2*= 1.80. (b) Original and fitted multifractal spectra; According to Peng et al. (2018), (α)min, (α)max, (Δα), (Δα)L, (Δα)R, (Δ)*f*, AI are the fractal parameters; (α)min and (α)max are α values corresponding to the maximum and minimum *q*, respectively; α0 is the value of (α) when *q* equals zero. (c) Mass exponent graph (or τ (*q*) curve); the value of moment *q* ranges from −8 to 9, with steps of 1. (d) Lacunarity distribution of the global fracture network shown on a (Λ(ε)) vs (ε) plot; local slopes plotted as d [log Λ(ε)]/d [log ε] against log (ε). (CDC: concave downward curve; CUC: concave upward curve).

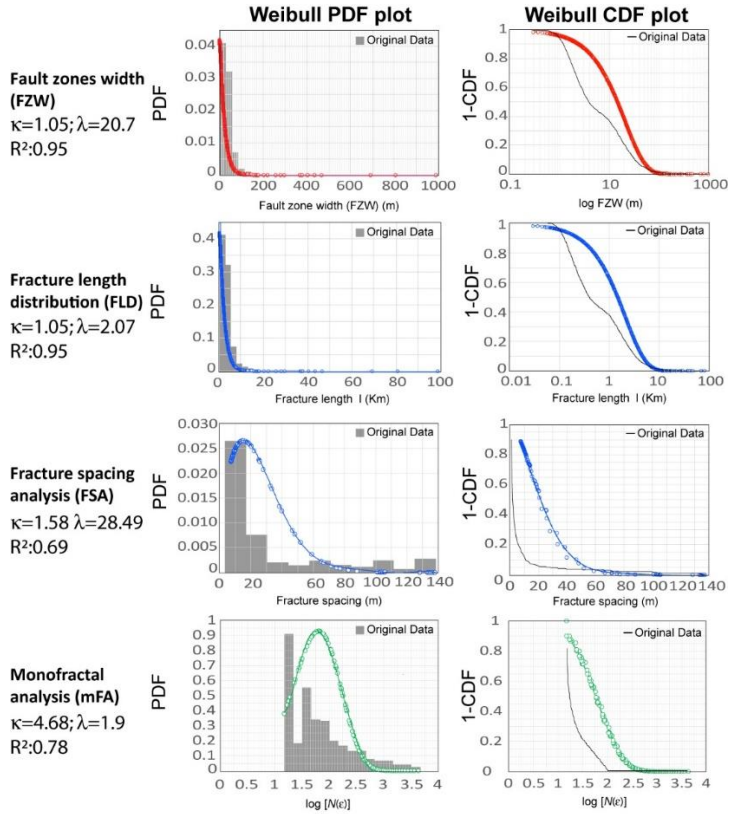

Fig 14. Probability density function (PDF) and survival distribution function (CDF) plots for Weibull distribution.

Table 5. Weibull distribution results for the geometrical parameters of fractures (κ is the shape parameter, λ is the scale parameter).

	κ	λ	Mean	Median	STDEV	Kurtosis	Skewness	Min.	Max.	Right tail	Left tail	Q1 (25%)	Q3 (75%)	R^2	Unit
Fault zones width (FZW)	1.05	20.7	25.21	14.33	51.98	143.04	10.11	0.29	988.3	65.24	0.29	28.96	4.61	0.95	m
Fracture length distribution (FLD)	1.05	2.07	2.52	1.43	5.2	143.05	10.11	0.029	98.83	6.52	0.03	2.90	0.46	0.95	Km
Fracture spacing analysis (FSA)	1.58	28.49	33.38	13.39	38.65	1.14	1.58	7.23	137.86	82.85	7.23	39.78	9.48	0.69	m
Monofractal analysis (mFA)	4.68	1.9	1.77	1.59	0.59	0.54	1.11	1.17	3.63	3.28	1.17	2.07	1.25	0.78	NA

6. Discussion

The fractal dimension does not completely define the geometry of the fracture system, and a complete characterization should include various geometrical attributes (e.g. fracture density, length distribution, fracture spacing, fracture orientation, roughness of the fracture surface, width, aperture and shear displacement) (Bonnet et al., 2001).

6.1. Fracture density

The curve of cumulative fracture density frequency for all fracture sets show a nonlinear behavior in a log-log plot and can be fitted by an exponential law (Fig 5b), this suggests that the fracture network is not strictly self-similar. Because, the fracture mapping is certainly not qualitatively uniform and the fracture network (Fig 3) is heterogeneous in terms of density (Fig 5a). According to Peacock and Mann (2005), the lithological competence, the tectonic setting and the stress regime can control the geometry and fractures density (Hashemi and Baizidi 2008). The strong fracturing densities observed are to be related to what they call fault damage zone. Damage zones structures includes *en echelon* extension fractures, antithetic and synthetic faults and rotated blocks with associated triangular openings at the intersections between faults. It is commonly assumed that fracture frequency increases in damage zones around faults (Wu and Groshong 1991; McGrath and Davidson 1995; Peacock 2001; Kim et al. 2004). The fracture density map (Fig 5A) shows the main zones of iso-fracturing in which the strong values are localised along the main faults, and consequently are considered as wall-damage zones.

6.2. Fracture length

Several fields studies have demonstrated that fracture populations have a power law length distribution (Davy et al. 1990; Davy 1993; Sornette et al. 1993; Pickering et al. 1995; Bour and Davy 1997 and 1999; Odling et al. 1999; Lasm 2000; Bonnet et al. 2001; Darcel et al. 2003a). The power law exponent (a) is generally in the range $1 < a < 3$ (Segall and Pollard 1983; Davy 1993; Berkowitz et al. 2000; Bonnet et al. 2001). According to Stoyan and Gloaguen (2011), the fit of statistical laws to empirical fracture distribution is difficult. This difficulty can be illustrated by a number of laws used to describe fracture process in the literature: power law (Velde and Dubois, 1991), exponential law (Villemin and Sunwoo, 1987), log-normal law (Castaing et al. 1995) and gamma law (Bonnet et al. 2001).

In this study, the resulting distribution function of fracture length obeys a logarithmic law (Fig. 8a). Cowie et al. (1993) found that the length distribution follows an exponential law during the first increments of deformation which, when fractures begin to interact, evolves toward a power law. It is recognized that resolution and finite size effects on a power law population can also result in distributions that appear to be exponential or lognormal (Bonnet et al. 2001). Davy (1993), in a study of over 5000 faults in the San Andreas system, demonstrated that the distribution of fracture lengths had Weibull tails for lengths greater than about 1000m. However,

for Lavenda (1995), the fracture length distribution follows the Fréchet distribution.

6.3. Fracture spacing

For the cumulative fracture spacing frequency distribution, the resulting distribution function Is close to exponential law (Fig 12b), that the fracture network of this area is not strictly self-similar with respect to fracture trace spacing for all fracture sets. According to Soliva et al. (2006), the nonfractal distribution justifies the use of scanlines. The coefficient of variation (*Cv*) calculated is 5.67, therefore, higher than 1 (Fig 10b). According to Odling et al. (1999) and Ackermann et al. (2001), if the fractures traces are clustered, the standard deviation of spacing is large and $Cv > 1$. Inversely, if the fractures are regularly spaced, the standard deviation is small and $Cv < 1$. The model defined by the scanline technique is confirmed by the coefficient of variation (*Cv*) which indicates a negative exponential distribution law (Fig 10c) and the clustered fractures model. Bonnet et al. (2001) discuss the relationship between the type of distribution of parameters such as the length, spacing and opening, and the stage of development of fracture networks. These authors demonstrate that undeveloped networks show an exponential law, while more mature networks follow a power law. Rives et al. (1992) concluded that fracture spacing destructions vary along different stage of fracture development. The distribution

is negative exponential at a stage with only few fractures, log-normal at intermediate fracture density, and tends toward normal at high fracture density. According to must publications the relative frequency of fracture spacing can be described by different distribution laws. Log-normal, normal, exponential, gamma and Weibull distributions were fitted to the spacing frequency histograms (Alizadeh et al. 2010). According to Hobbs et al. (2022), the Fréchet or Weibull distribution are to be expected from current theories of fracture spacing. Boadu and Long (1994), in a study of fracture spacings in Lake Strom Thurmond, (Georgia, U.S.A) showed that the distribution of fracture spacings follow a fractal and Weibull distribution which implies that they were formed as a result of a repetitive fragmentation process.

6.4. Monofractal analysis

According to Lasm (2000), for the monofractal analysis (mFA), and the multifractal analysis (MFA) the high values of *Db* observed (eg. in our case: *Db*=1.56 and *D1*=1.81, respectively) (Figs 11 and 12), can be attributed to the structural complexity of the fracture network which indicates the presence of more than one phase of deformation in the study area (Boudjema 1987), and *Db* depends on fracture density, rather than clustering (Berkowitz and Hadad 1997).

Using computer simulations of fracture networks, La pointe (1988) suggests that the fractal dimension is most sensitive to the fractures number (*n*) of or cells size (ε), rather than their length (*l*) variability, and orientation (*Ot*). According to Zazoun (2008), the difference in the fracturing density observed in the Fadnoun region (Fig 1a), obtained by performing a monofractal analysis for three sectors; a northwestern sector, a central sector and a southeastern sector, the fractal dimension D*b* calculated are respectively equal to 1.84, 1.91 and 1.94. Indeed, the change of the fractal dimension from one sector to another observed by this author has shown that the fractal object is inhomogeneous or multi-fractal, hence the need to have undertaken a multifractal analysis. Using the box-counting method (BCM), Djezzar et al. (2020) examine the fracture network in the Mouydir region, located to the west of the study area (Fig 1a), and obtain a monofractal dimension (D*b*) of 1.57. The fracture length distribution analysis by these authors showed a value of the power-law exponent (*a*) equal to 2.89. According to Liu et al. (2015 and 2016), when *Db* (or *D1*) exceeds a particular value (>1.5), the flow rate distribution becomes more uniform, and shorter fractures dominate the preferential flow paths. Thus, the fracture permeability become more stable. The observed greater values of the power-law exponent (*a*) of the fracture length distribution indicate that short fractures are more important in strain accommodation than long fractures (Ackermann et al. 2001). In the study area, the cumulative fracture length distribution shows a smaller value of (*a*) (=0.44) (Fig 8) and the *Db* values equal to 1.56 and 1.81, respectively for the monofractal and the multifractal analyses (Figs 11 and 13), which allows one to consider the opposite observation of these authors. Thus, short fractures are less important in strain accommodation than long fractures. The spatial distribution of fractures using the box-counting method is respectively consistent with a fractal character ($1 \leq Db \leq 2$) and obey a power law function (Fig 10), and this is in relevance to all directions and all fracture lengths confounded over the whole study area (Figs 1 and 3).

According to Bonnet et al. (2001), a fractal network is defined as a spatial correlation and organization between fractures that can be quantified using the fractal dimension, and is independent of the distributions of other fracture traces. On the other hand, the fractures may be arbitrarily distributed in space (i.e., nonfractal), whereas other fracture characteristics, such as length, spacing or orientation, may follow power law distributions (Bour and Davy, 1997). For the pairs $[\varepsilon, N(\varepsilon)]$, reported in Figure 11, the points fall into a straight line from an (ε) value of more than 30m and in Figure 7, the fit by a power law is valid for a fracture length of more than 108.54 m and for a fracture spacing of more than 3m. The causes of behavioral tendency have been recalled by Velde and Dubois (1991), Gillespie et al. (1993), Bodin and Razack (1999) and Zazoun (2008). According to these authors, these restrictions can be explained by several factors, such as the limit of photogeological resolution of the sampling data method or the lower break reached up scale. Unfortunately, the concepts of truncation and censoring artifacts cloud all the interpretations with no attempt to show us that these artifacts actually exist (Clark et al. 1999). This is to be expected since the standard box counting procedure for spatial data points is a way of determining a nearest neighbour distribution which is by definition a Weibull distribution (Hobbs et al. 2022).

6.5. Multifractal analysis

The multifractal dimension of the most intensive clustering in the heterogeneous set is represented by the value $D9=D\infty$. The maximum value of $D(q)$=1.84, corresponds to q equal to -8, while The minimum value of $D(q)$ = 1.73, corresponds to q equal to 9. The generalised dimension $D(q)$ showed a slow rate decrease in relatively homogeneous samples, leading to a convergence toward a constant value for moments $q \geq 0$ (Fig 13). According to Jouini et al. (2011), this observation confirms that generalised dimensions $D(q)$ can be used to determine the degree of data heterogeneity. Effectively, the low value of the difference D0-D1 (=0.03) and the ratio D1/D0 (=0.98) near 1 observed indicate a low degree of fracture density (Fig 5a). The Renyi dimensions (*D0, D1,* and *D*2) (Feder 1988), show respectively, 1.84, 1.81, and 1.80. The dimensions (D0, D1, and D2) remain quite close in values, which indicates that the fractures network is probably monofractal.

The fractal spectra $f(\alpha)$ from multifractal analysis (MFA) reveals an asymmetric parabola (Figs 11 and 12). According to Liu et al. (2001), this would reflect a variability in the lengths of observed fractures. The value of the amplitude difference (Δf) observed between the values of $f(\alpha)$ at αmax and αmin for the multifractal analysis is equal to 0.51 and the multifractal spectra $f(\alpha)$ shows an asymmetrical curve, with a left deviation, and the asymmetrical index AI is equal to -0.57 (left-hook curve) (Fig 13b). According to these authors, when the asymmetry (Δf) > 0, which reveals that the fractures with longer lengths were more common than shorter fractures and the fractures are medium-small scale and are discontinuous in space (Fig 4b and 5a). The calculated value of $\Delta\alpha$ is equal to 0.94. According to Biswas et al. (2012), a large value for $\Delta\alpha$, indicates a multifractal behavior. The fracture networks are well known for displaying self-similarity in many circumstances, and their connection and flow behavior are influenced by their fractal dimensions (Roy et al. 2006).

6.6. Fracture connectivity

Bour and Davy (1997), Bonnet et al. (2001) and Darcel et al. (2003b) have shown that the connectivity of the fracture networks depends on the power law exponent (*a*) and on the fracture density. Berkowitz et al. (2000) analyzed the fracture connectivity on the light of relation of exponent (*a)* to capacity fractal dimension *D0*, for *a>D0*, the connectivity does not depend of scale, inversely for *a*<D*0*, the connectivity threshold is reached only at a critical value. In the study area, with *a= 5.79* and *D0=1.84* (Tables 1 and 2), it is attempting to say that fracture connectivity is largely independent on scale. In some cases, where large damage area develops as displacement accumulates, both the fractal dimension and connectivity may increase together because the area of damage zone is controlled by the extent of slip (de Joussineau and Aydin 2007; Park et al. 2010). The lacunarity value ($\Lambda(\varepsilon)$) calculated ranges $0.07 < (\Lambda(\varepsilon)) < 5.90$., because the value of the lacunarity is not a constant but depends heavily on the size and density of the sampling box (Wu et al., 2013). As noted by Plotnick et al. (1996), when the fractal object is homogeneous and invariant by translation, the lacunarity is of very low value in the presence of relatively low size gaps. Conversely, it takes an important value for large size gaps for a heterogeneous and non-translationally invariant geometric objects. This heterogeneity can be observed on the isodensity fracturing map (Fig 5a) and it results in a clustered fracture patterns, underlined by a negative exponential distribution law for spacing distribution (Fig 10c). The lacunarity ($\Lambda(\varepsilon)$) decreases for increasing (ε) (Fig 13d). According to Marwan et al. (2007), because larger boxes will be more translationally invariant than smaller boxes. Figure 13d shows that global fracture network presents a higher lacunarity exponent (-2.13). The greater beta lacunarity exponent confirms greater heterogeneity in the distribution of fractures. While, the lower beta exponent of lacunarity indicates more uniform fracture distribution. Additionally, a concave downward lacunarity curve (CDC) represent fracture network that are composed of clustered fractures and have high lacunarity. Conversely, concave upward curve (CUC) shows fracture network fracture with randomly distributed gaps and low lacunarity values. Figure 13d shows the local slopes of the log ($\Lambda(\varepsilon)$) versus log ε curve calculated at each ε and denoted by d [log Λ)]/[d(log ε)]. It can be seen from this figure that the fracture network behaves like the multifractal pattern and displays somewhat of a "flat segment" in the d[log Λ)]/[d(log ε)]versus log ε plot. Such observations have been corroborated by the studies of Plotnick et al. (1996) and Roy and Perfect (2014).

6.7. Fractal anisotropy

Our study shows that the orientation of Dh*max* (N067°) is close to the maximum stress tensor axis orientation (σ1: N040°), recorded during the Hercynian compressional event (Boudjema 1987) and the main orientation of fractures (Fig 12). As a result, the fractal ellipse displays a spatial-temporal directional connection between the maximum stress tensor (σ1) and the fracture pattern produced. By using a 1-D fracture profile on transect, it is possible to determine the fractal anisotropy (FA) of spatial fracture distribution, active during a paleostress field, and this appears to be a valuable method to characterize the geometrical and structural configurations resulting from fracture patterns (Pérez-López et al. 2005 and 2007). In their study of the Variscan granitic massif *''El Berrocal''* in the Gredos Mountain Range of Spain, Pérez-López and al. (2005) and Pérez-López and Paredes (2007) show a relationship between the fractal anisotropy ellipse of the spatial faults distribution and the paleostress field, i.e. that the orientation of σ1 is normal to the orientation of Dh*max*. In our study, the N040° Hercynian maximum stress tensor (σ1) is expected to be normal to Dh*max* (N067°). Unfortunately, a large deviation of 63° between these two parameters was observed (Fig 12), this would probably be the result of a fracturing mechanism occurring during the different geological tectonic events emphasizing the superposition of the phases of fractures generation. Indeed, the cause of fractal characteristics depends on the formation and development of tectonic processes (Liu et al. 2021).

7. Conclusions

The fracture study carried out in the Tassili-n-Ajjers area from the analysis of fracture density by the box counting method shows a single fractal character and the Weibull distribution for the monofractal analysis. The spacing law between the fractures direction shows a negative exponential distribution consistent with the clustered fractures model. The syn-fault fractures tend to

increase in frequency near the faults and we interpret the strong fracture density as damage zones. The curves of cumulative length frequency and the fracture orientation shows a nonlinear behavior and can be fitted by a logarithmic law. The cumulative fracture spacing frequency of fracture traces, the fracture density and the fracture connectivity distributions for all fracture obey an exponential law function. Basically, the geometrical parameters of fractures are scale dependent and should be approximated by a classical distribution laws. However, the Weibull distribution remains more appropriate, especially with regard to fractal analysis by the box counting method (BCM). The data analyses reveal that multifractal and lacunarity informations provides a more comprehensive understanding of the spatial heterogeneity of fracture network than any monofractal dimension.

Acknowledgements
We would like to thank Sonatrach-Algeria for providing logistical support for fieldwork in 2000 and 2002. We thank Bruce E. Hobbs (University of Western Australia) and Soumyajit Mukherjee (IIT Bombay) for their constructive criticism. This work is dedicated to the memory of Prof. Yamina Mahdjoub.

Appendix A1. Overview of fracture definition

A natural fracture is a term adopted for planar macroscopic discontinuity, as a result of brittle failure in the presence of an imposed stress field (Nosjean et al. 2020). Fractures within the rock are shown as veins, joints, and faults, and they exist at a different variety of scales, from the microscopic scale to the macroscopic one. The fracture description requires a concept prioritization, namely from the most elementary (the individual fracture or fracture set) to intermediaries who are the fractures' family, then the fractures' system, and up to the more global network (Macé 2008). Fractures that belong to the identical system are the consequence of the application of the same stress field (National Research Council 1996). In outcrops, the fractures appear as continuous and straight traces bearing no traces of displacement (Cacas et al. 2001). The fracture networks organization (FNO) is often divided into two groups (Rives et al. 1992; Cacas et al. 2001; Putot et al. 2001; Sanderson and Peacock 2019):

(1) Systematic fracture networks (SFN), whose fracture networks is regular in terms of spacing and orientation (see Appendix A1. Figs 1a-b and 2a).

(2) fracture corridor or fracture cluster (Fc), which are spatially heterogeneously distributed. They are usually associated with fault zones and occur with strong sub-vertical development (swarm) (Zazoun 2008; Matar et al. 2010; Nosjean et al. 2020) (see Appendix A1. Fig 1c-d and 2a).

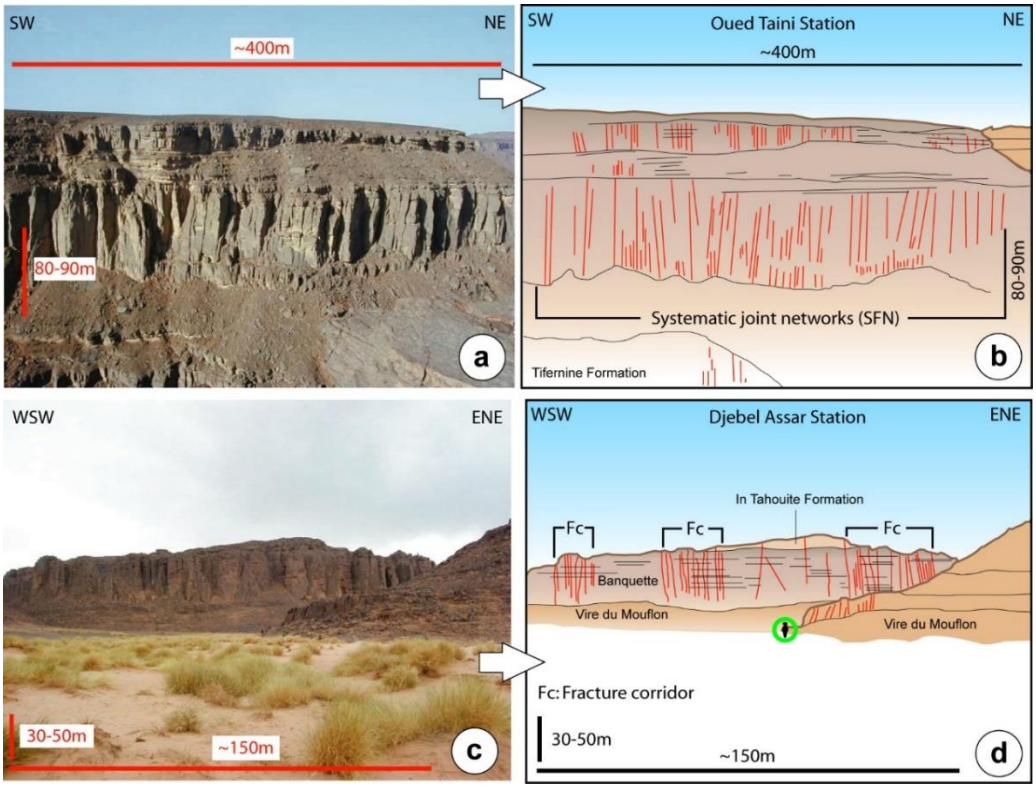

Fig A1. 1. Photographs showing fracture network geometry in the Tassili-n-Ajjers area: (a-b) Systematic fractures observed in the Silurian sandstones (Tifernine formation ''Silurian'', Oued Taïni station; X: 08° 03' 490 E / Y: 25° 44' 180 N). (c-d) Fracture swarms in Ordovician sandstones (Cambro-ordovician formations, Djebel Assar station; X: 08° 26' 82" E / Y: 25° 10' 57" N).

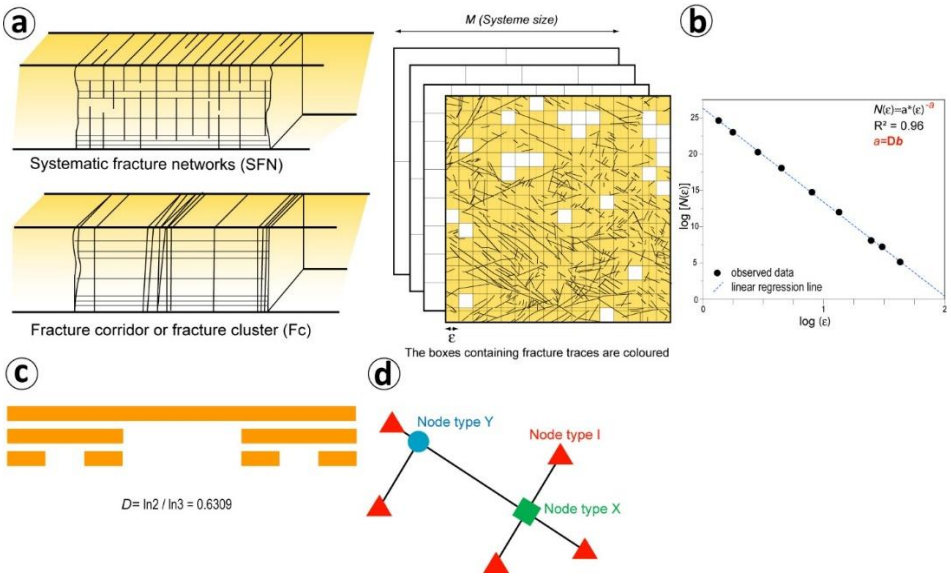

Fig A1. 2. (a) The fracture networks organization (FNO): Systematic fracture networks (SFN) and fracture corridor or fracture cluster (Fc) (Modified from Bazalgette 2004). (b) The box-counting method (BCM) measuring the fractal dimension by superimposing a sequence of regular meshes with different cell sizes (ε) over the fracture map (*M*) and counting the number of occupied boxes *N*(ε). The fractal dimension (*a*=D*b*) is derived as the negative slope of the linear regression line of data points (*ε, N*) plotted in logarithmic axes (Lei et al. 2014). The multifractal analysis (MFA) derived from the box-counting method for which each box of size (*ε*) is weighted by the total length (*Li*) included in it (Bonnet et al. 2001). (c) Cantor's Dust Method (CDM): The solid line of unit length is divided into 3 parts, r=1/3, and the center third is removed, the process is repeated. The Cantor dust has a fractal dimension (D) between 0 and 1 (From Turcotte 1989) (d) Classification of node types. X type: fractures are crossed, I type: fracture start and end, Y type: fracture abutment with another fracture (Modified from Sanderson and Nixon 2015).

Appendix A2. Weibull distribution

In probability theory and statistics, the Weibull distribution is a continuous probability distribution (https://en.wikipedia.org/wiki/Weibull_distribution).

The Weibull distribution (Weibull 1951) and theory have found many applications in reliability and fracture theory (Bažant and Planas 1998; Krajcinovic, 1996; Munz and Fett, 2001), and it is one of the best-known lifetime distributions. It describes observed failures of many different types of components and phenomena (Brandt 2019).

The two common forms of the Weibull distribution forms of the distribution function are as follows:

The formula for the probability density function (PDF) of the general Weibull distribution is: (Eq. A2.1) (Figs A2. 1).

$$f(x) = \frac{k}{\lambda}\left(\frac{x-\mu}{\lambda}\right)^{(k-1)} \exp(-(((x-\mu)/\lambda)^k) \quad x \geq \mu; k, \lambda > 0 \quad \text{(A2.1)}$$

The formula for the cumulative distribution function (CDF) of the general Weibull distribution is: (Eq. A2.2) (Figs A2. 1).

$$F(x) = 1 - e^{-(x/\lambda)^k} \quad x \geq 0;\ k > 0 \quad \text{(A2.2)}$$

Where κ is the shape parameter, also know the Weibull slope or the threshold parameter, λ is the scale arameter, also called the characteristic life parameter and μ is the location parameter or the shift parameter.

The Weibull distribution includes the exponential (κ = 1) and the Rayleigh distribution (κ = 2) as special cases.

According to Brandt (2019), the shape parameter (κ) determines the class of failure mode:

A value of $\kappa < 1$ indicates that the failure rate decreases over time.

A value of $\kappa = 1$ indicates that the failure rate is constant over time.

A value of $\kappa > 1$ indicates that the failure rate increases with time.

A value of $\kappa > 4$ indicates that the failure rate rapidly increases with time

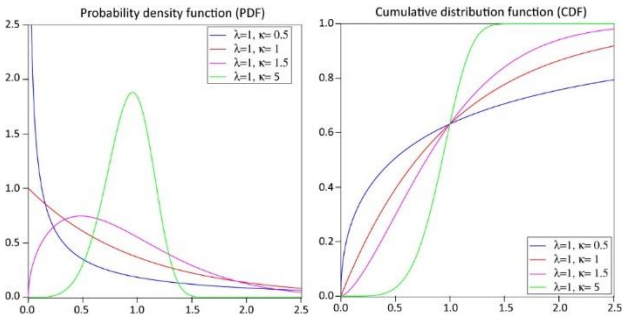

Fig A2. 1. Probability density function (PDF) and cumulative distribution function (CDF) plots for Weibull distribution (After Leitch, 2010 https://en.wikipedia.org/wiki/Weibull_distribution)

References

Ackermann RV, Schlische RW, Withjack M (2001) The geometric and statistical evolution of normal fault systems: an experimental study of the effects of mechanical layer thickness on scaling laws, *Journal of Structural Geology* 23: 1803–1819.

Afshari Moein MJ, Valley B, Tvans KF (2019) Scaling of Fracture Patterns in Three Deep Boreholes and Implications for Constraining Fractal Discrete Fracture Network Models, *Rock Mechanics and Rock Engineering* 52: 1723-1743.

Agterberg FP, Cheng Q, Brown A, Good D (1996) Multifractal modeling of fractures in the Lac du Bonnet batholith, Manitoba, *Computer and Geosciences* 22(5): 497–507.

Alizadeh H, Rahimi B, Golyan MF (2010) Statistical and fractal analysis of the fractures in Derakht-e-Bid Tonalite, West of Mashhad, North-East Iran. The 1st International Applied Geological Congress, Department of Geology, Islamic Azad University - Mashad Branch, Iran, 26-28 April 2010.

Allain C, Cloitre M (1991) Characterizing the lacunarity of random and deterministic fractal sets, *Physical Review* A 44: 3552–3558.

Allègre JC, Lemouel JL, Provost A (1982) Scaling rules in rock fracture and possible implications for earthquake prediction, *Nature* 297: 47–49.

Andrews BJ, Roberts JJ, Shipton ZK, Bigi S, Tartarello MC, Johnson G (2019) How do we see fractures? Quantifying subjective bias in fracture data collection, *Solid Earth* 10: 487–516.

Aviles CA , Scholz CH, Boatwright J (1987) Fractal analysis applied to characteristic segments of the San Andreas fault, Journal of Geophysical Research 92 : 331–344.

Baka D, Lasm T, Yao TK, Oga M-S, Youan TAM, De Lasme OZ (2014) Analysis of the fracture network extracted from radar images of the Precambrian basement of the Oumé region (center-west of Ivory Coast), *Photo-Interpretation European Journal of applied Remote sensing* 50 : 142-159.

Balberg I, Berkowitz B, Drachsler GE (1991) Application of a percolation model to flow in fractured hard rocks, *Journal of Geophysical Research* 96B: 10015–10021.

Balberg I, Binenbaum N (1983) Computer study of the percolation threshold in a two-dimension anisotropic system of conducting sticks, *Physical Review* 28: 3799–3812.

Barton CC, Hsieh PA (1989) Physical and hydrological-flow properties of fractures International Geological Congress Environmental Engineering and Urban Geology United States 2- Field Trip Guidebook T385, Washington DC, USA.

Barton CC, Hsieh PA, Angelier J , Bergerat F , Bouroz C , Dettinger MD, Weeks E (1989) Physical and hydrological-flow properties of fractures: Las Vegas Nevada-Zion Canyon Utah-Grand Canyon Arizona-Yucca Mountain Nevada-Field Trip Guidebook T 385. American Geophysical Union Editions, Washington DC, USA.

Barton CC, Larsen E (1985) Fractal geometry of two-dimensional fracture networks at Yucca Mountain south-western Nevada. Proceedings of the International Symposium on Fundamentals of Rock Joints, Bjorkliden, Sweden.

Bazalgette L (2004) Multi-scale folding / fracturing relationships in sedimentary multilayers in the elastic / brittle domain: Discontinuous accommodation of curvature by small-scale fracturing and by joints. Possible dynamic implications in reservoir flows, PhD Thesis, Montpellier II University, France (in French).

Bažant Z P, Planas J (1998) Fracture and Size Effect in Concrete and other Quasibrittle Materials, CRC Press, Washington DC.

Berkowitz B, Hadad A (1997) Fractal and multifractal measures of natural and synthetic fracture networks, Journal *of Geophysical Research* 102: 12205-12218.

Berkowitz B, Bour O, Davy P, Odling N (2000) Scaling of fracture connectivity in geological formations, *Geophysical Research Letters* 27: 2061–2064.

Beuf S, Bennacef A, Biju-Duval O, de Charpal O, Gariel O, Rognon P (1968) The great sedimentary complexes of the Lower Paleozoic of the Sahara, *Comptes Rendus Sommaire de la Société Géologique de France* 8 : 260–263 (in French).

Beuf S, Biju-Duval B, De Charpal D, Rognon R, Bennacef A (1971) Lower Paleozoic sandstones in the Sahara Sedimentation and discontinuity: structural evolution of a craton, Technip Editions, Sciences et Techniques du Pétrole Institut Français du Pétrole (in French).

Biswas A, Cresswell HP, Bing Si (2012) Application of Multifractal and Joint Multifractal Analysis in Examining Soil Spatial Variation: A Review, Fractal Analysis and Chaos in Geosciences, IntechOpen Limited, London, UK.

Blenkinsop TG (1994) The fractal distribution of gold deposits-Fractals and Dynamic Systems in Geosciences, Springer Berlin, Germany.

Blenkinsop TG Sanderson DJ (1999) Are gold deposits in the crust fractals? A study of gold mines in the Zimbabwe craton, Fractures Fluid Flow and Mineralization, *Geological Society Special Publication* 155: 141–151.

Boadu FK, Long LT (1994) Statistical distribution of natural fractures and the possible physical generating mechanism. *pure and applied geophysics* 142 : 273-293.

Bodin J, Razack M (1999) Image analysis applied to the automatic processing of fracture fields. Geometric properties and scale laws, *Bulletin de la Société Géologique de France* 170 : 579-593 (in French).

Bonneau F (2014) Inclusion of indirect data in the simulation of discrete fracture networks, PhD Thesis, University of Lorraine, France (in French).

Bonnet E, Bour O, Odling NE, Davy P, Main IG, Cowie PA, Berkowitz B (2001) Scaling of fracture systems in geological media, *Reviews of Geophysics* 39: 347-383.

Borroco J, Nyssen R (1959) New observations on the 'Lower Cambro-Ordovician' sandstones of inner Tassili (North Hoggar), *Bulletin de la Société Géologique de France* 2: 197–206 (in French).

Boudjema A (1987) Structural evolution of the "Triassic" oil basin of the North Eastern Sahara (Algeria), PhD Thesis, Paris XI-Orsay University, France (in French).

Bour O, Davy P (1997) Connectivity of Random Fault Networks Following a Power-Law Fault Length Distribution, Water *Resources Research* 33: 1567-158.

Bour O, Davy P (1999) Clustering and size distributions of fault patterns: theory and measurements, Geophysical *Research Letters* 26: 2001–2204.

Bour O, Davy P, Darcel C, Odling N (2002) A statistical scaling model for fracture network geometry with validation on a multiscale mapping of a joint network (Hornelen Basin Norway), Journal of Geophysical Research 107: 1-13.

Bouroz C (1990) Joints and their tectonic significance in the tabular domain: example of the Colorado Plateau (Utah Arizona, New Mexico), PhD Thesis, University Paris VI (in French).

Brandt M B C (2019) Weibull failure analysis of seismic event return periods in the Far West Rand and Klerksdorp-Orkney-Stilfontein-Hartebeesfontein gold mine areas, *The Journal of the Southern African Institute of Mining and Metallurgy* 119: 995-1003.

Cacas MC, Daniel JM, Letouzy J (2001) Nested geological modeling of naturally fractured reservoirs, *Petroleum Geoscience* 7: 43–52.

Cao J, Fang X, Na J, Tang G (2017) Study on the characteristics of the topographic relief of shoulder line of different geomorphic types in Loess Plateau based on multi-fractal, *Geographic Geo-Information Science* 33: 51–56.

Carpena P, Coronado AV (2019) Connection of the nearest-neighbour spacing and the local box-counting dimension for discrete sets, *Physical Revue E*: 100, 022205.

Castaing C, Genter A, Ouillon G (1995) Multiscale organization of joints and faults revealed by geostatistical, multifractal and wavelet techniques, *American Association of Petroleum Geologists Bulletin* 79: no CONF-950995.

Cello G (1997) Fractal analysis of a Quaternary fault array in the central Apennines, Italy, *Journal of Structural Geology* 19: 954-953.

Cheng Q (1999) The gliding box method for multifractal modeling, *Computers & Geosciences* 25: 1073-1079.

Chilès JP (1988) Fractal and geostatistical methods for modeling of a fracture network, *Mathematical Geosciences* 20: 631–654.

Choi J-H, Edwars P, Ko K, Kim Y-S (2016) Definition and classification of fault damage zones: A review and a new methodological approach, *Earth-Sciences Revue* 152: 70-87.

Claracq P, Fabre C, Freulon J M, Nougadère F (1958) An angular unconformity in the lower sandstones of the Adrar Tan Elak (central Sahara), *Comptes Rendus de la Société Géologique de France* : 309-310 (in French).

Clark RM, Cox SJD, Laslett GM (1999) Generalizations of power-law distributions applicable to sampled fault-trace lengths: model choice, parameter estimation and caveat, *Geophysical Journal International* 136 (2): 357-372.

Cowie PA, Vanneste C, Sornette D (1993) Statistical physics model for spatiotemporal evolution of faults, *Journal of Geophysical Research* 98: 21809–21822.

Cox DR, Lewis PAW (1966) The Statistical Analysis of Series of Events, Methuen & Co Limited Editions, London, UK.

Craig J, Rizzi S, Said F, Thusu B, Luning S, Asbali AI, Keeley ML, Bell J F, Durham MJ, Eales MH, Beswetherick S, Hamblett C (2008) Structural styles and prospectivity in the Precambrian and Palaeozoic hydrocarbon systems of North Africa, The Geology of East Libya Gutenberg Press, Malta.

Darcel C, Bour O, Davy P (2003a) Stereological analysis of fractal fracture networks, *Journal of Geophysical Research* 108: 1-15.

Darcel C, Bour O, Davy P, DE Dreuzy JR (2003b) Connectivity properties of two dimensional fracture networks with stochastic fractal correlation, *Water Resources Research* 39: 1272-1285.

Davy P (1993) On the fault-length frequency distribution of the San Andreas fault system, *Journal of Geophysical Research* 98: 141-151.

Davy P, Sornette A, Sornette D (1990) Some consequences of a proposed fractal nature of continental faulting, *Nature* 348: 56-58.

de Joussineau G, Aydin A (2007) The evolution of the damage zone with fault growth in sandstone and its multiscale characteristics, *Journal of Geophysical Research* 112: 1-20.

De Souza J, Rostirolla SP (2011) A fast MATLAB program to estimate the multifractal spectrum of multidimensional data: Application to fractures, *Computers & Geosciences* 37: 241-249.

Delogkos E, Manzocchi T, Childs C, Camanni G, Roche V (2020) The 3D structure of a normal fault from multiple outcrop observations, *Journal of Structural Geology* 136: 104009.

Deng J, Wang Q, Wan L, Liu H, Yang L, Zhang J (2011) A multifractal analysis of mineralization characteristics of the Dayingezhuang disseminated-veinlet gold deposit in the Jiaodong gold province of China, *Ore Geology Reviews* 40: 54-64.

Dershowitz WS, Einstein HH (1988) Characterizing rock joint geometry with joint, *Rock Mechanics and Rock Engineering* 21: 21–51.

Djezzar S, Rasouli V, Boualam A, Rabiei M (2020) An integrated workflow for multiscale fracture analysis in reservoir analog, *Arabian Journal of Geosciences* 13: 161 3-27.

Ehlen J (2000) Fractal analysis of joint patterns in granite, *International Journal of Rock Mechanics and Mining Sciences* 37: 909-922.

Eschard R, Hussein A, Braik F, Desaubliaux G (2005) The Lower Paleozoic succession in the Tassili outcrops Algeria: sedimentology and sequence stratigraphy, *First Break* 23: 27-35.

Evertsz CGC, Mandelbrot B (1992) Multifractal Measures, Chaos and Fractals Springer Verlag, Germany.

Fabre J (2005) Geology of Western and Central Sahara, Royal Museum of Central Africa, Tervuren, Belgium (in French).

Faulkner DR, Lewis A, C Rutter EH (2003) On the internal structure and mechanics of large strike-slip fault zones: field observations of the Carboneras fault in southeastern Spain, *Tectonophysics* 367: 147–156.

Feder J (1988) Fractals Plenum Press New York, USA.

Fekirine B, Abdallah H (1998) Palæzoic lithofacies correlatives and sequence stratigraphy of the Saharan platform Algeria, Petroleum Geology of North Africa, *Geological Society of London Special Publication* 132: 97-108.

Felici F, Alemanni A, Bouacida D, de Montleau P (2016) Fractured reservoir modeling: From well data to dynamic flow Methodology and application to a real case study in Illizi Basin (Algeria), *Tectonophysics* 690: 117-130.

Galeazzi S, Point O, Haddadi N, Mather J, Druesne D (2010) Regional geology and petroleum systems of the Illizi-Berkine Area of the Algerian Saharan Platform, *Marine and Petroleum Geology* 27: 143–178.

Gander W, Strebel R, Golub GH (1995) Fitting of circles and ellipses least squares solution, *SVD and Signal Processing III Algorithms Architectures and Applications* 34: 349-356.

Gauthier BDM, Lake SD (1993) Probabilistic modeling of faults below the limit of seismic resolution in Pelican field, North Sea, offshore United Kingdom, *American Association of Petroleum Geologists Bulletin* 77: 761–777.

Gerik A, Kruhl JH (2009) Towards automated pattern quantification: Time-efficient assessment of anisotropy of 2D patterns with AMOCADO, *Computers & Geosciences* 35: 1087-1097.

Giaquinta A, Boccaletti S, Boccalettti M, Piccardi L, Arrechi FT (1999) Investigating the fractal propreties of geological fault systems: The Main Ethiopian Rift case, *Geophysical Research Letters* 26, 11: 1633-1636.

Gillespie PA, Howard CB, Walsh JJ, Watterson J (1993) Measurement and characterisation of spatial distributions of fractures, *Tectophysics* 226: 113–141.

Giri A, Tarafdar S, Dutta T (2016) Relation between Lacunarity Correlation dimension and Euclidean dimension of Systems, *arXiv 160206293:* 1-24.

Guiraud R, Bosworth W, Thierry J, Delplanque A (2005) Phanerozoic geological evolution of Northern and Central Africa: An overview, *Journal of African Earth Sciences* 43: 83-143

Guiraud R, Doumnang Mbaigane J-C, Carretier S, Dominguez S (2000) Evidence for a 6000 km length NW–SE-striking lineament in northern Africa: the Tibesti Lineament, *Journal of Geological Society of London Special Publication* 157 : 897–900.

Gupta A, Scholz CH (2000) Brittle strain regime transition in the Afar depression: implications for fault growth and seafloor spreading, *Geology* 28: 1087–1090.

Haddoum H, Guiraud R, Moussine-Pouchkine A (2001) Hercynian compressional deformations of the Ahnet-Mouydir Basin Algerian Saharan platform: far-field stress effects of the Late Palæozoic Orogeny, *Terra Nova* 13: 220–226

Halsey TC, Jensen MH, Kadanoff LP, Procaccia I, Shraiman BI (1986) Fractal measures and their singularities: the characterization of strange sets, Physical Review A33 1141-1151.

Hanks CL, Lorenz J, Lawrence T, Krumhardt AP (1997) Lithologic and structural controls on natural fracture distribution and behavior within the Lisburne Group northeastern Brooks Range and North Slope subsurface Alaska, *American Association of Petroleum Geologists Bulletin* 81: 1700-1720.

Hashemi S N, Baizidi C (2018) 2-D Density and Directional Analysis of Fault Systems in the Zagros Region (Iran) on a Regional Scale, *Pure and Applied Geophysics* 175: 2753-2768.

Healy D, Rizzo RE, Cornwell DG, Farrell NJ C, Watkins H, Timms NE, Gomez-Rivas E, Smith M (2017) FracPaQ: A MATLAB™ toolbox for the quantification of fracture patterns, *Journal of Structural Geology* 95: 1-16.

Hentschel HGE, Procaccia I (1983) The infinite number of generalized dimensions of fractals and strange attractors, *Physica* D8: 435-444.

Hirata T (1989) Fractal dimension of fault systems in Japan: Fractal structure in rock fracture geometry at various scales, *Pure and Applied Geophysic* 121, 157–170.

Hobbs BE, Ord A, Blenkinsop T (2022). The spatial distributions of mineralization, *Journal of Structural Geology* 156: 104529.

Hudson JA, Priest SD (1983) Discontinuity frequency in rock masses, *International Journalof Rock Mechanics and Mining Science & Geomechanics Abstracts* 20: 73-89.

Joarder A, Krishna H, Kundu D (2011) Inferences on Weibull parameters with conventional type-I censoring, *Computational Statistics & Data Analysis* 55 (1) : 1-11.

Jouini M, Vega S, Mokhtar EA (2011) Multiscale characterization of pore spaces using multifractals analysis of scanning electronic microscopy images of carbonates, *Nonlinear Processes in Geophysics* 18: 941-95.

Karperien A (2004) Using FracLac V 20f for ImageJ: FracLac Advanced User's Manual Charles Sturt University Australia 1-38, https://imagej,nih,gov/ij/plugins/fraclac/fraclac-manual,pdf, Software available from https://imagej,nih,gov/ij/plugins/fraclac/FLHelp/Introduction,htm.

Khider M (2011) Multifractal analysis by 2D MMTO: Evaluation on radar and medical images, PhD Thesis, USTHB Algiers, Algeria (in French).

Kim Y-S, Peacock DCP, Sanderson DJ (2004) Fault damage zones, *Journal of Structural Geology* 26: 503–517.

Korvin G (1992) Fractal models in the earth sciences, Elsevier Science Ltd Amsterdam, The Netherlands.

Krajcinovic D (1996) Damage Mechanics, North-Holland Series in Applied Mathematics and Mechanics, Elsevier, Amsterdam.

Kruhl JH (2013) Fractal-geometry techniques in the quantification of complex rock structures: a special view on scaling regimes inhomogeneity and anisotropy, *Journal of Structural Geology* 46: 2–21.

Krumbholz M, Hieronymus C, Burchardt S, Troll VR, Tanner DC, Friese N (2014) Weibull-distributed dyke thickness reflects probabilistic character of host-rock strength, *nature communications* 5: 3272.

La Pointe P (1988) A method to characterize fracture density and connectivity through fractal geometry, *International Journal of Rock Mechanics and Mining Sciences & Geomechanics Abstracts* 25: 421-429.

Lasm T (2000) Hydrogeology of basement fractured reservoirs: Statistical and geostatistical analyzes of fracturing and hydraulic properties Application to the Mountain Region of Ivory Coast (Archean Domain), PhD Thesis, Poitiers University, France (In French).

Latrèche S (1982) Structural evolution of the Illlizi basin (Eastern Algerian Sahara) in the Upper Paleozoic, Master of Sciences, Aix-Marseille University, France (In French).

Lavenda BH (1995) Thermodynamics of Extremes. Albion Publishing, Chicester.

Lei Q, Latham J-P, Xiang J, Lang P (2014) Representation of large scale network geometry with realistic apertures determined by mesoscale geomechanical modelling of a natural fracture system, 48 th US Rock Mechanics, Geomechanics Symposium held in Minneapolis MN, USA.

Liu R, Jiang Y, Li B, Jiang Y (2016) A fractal model based on a new caverning equation of fluid flow in fractures for characterizing hydraulic properties of rock fracture networks, *Computers and Geotechnics* 75: 57-68.

Liu R, Jiang Y, Li B, Wang X (2015) A fractal model for characterizing fluid flow in fractured rock masses based on randomly distributed rock fracture networks, *Computers and Geotechnics* 65: 45-55.

Liu Z, Han L, Du C, Cao H, Guo J, Wang H (2021) Fractal and Multifractal Characteristics of Lineaments in the Qianhe Graben and Its Tectonic Significance Using Remote Sensing Images, *remote sensing* 13: 2-26.

Lochmann K, Gloaguen R, Stoyan, D (2007) Geometrical-statistical modelling of systems of fracture zones along oceanic ridges, *Geophysical Journal International* 170 (2): 605–614

Macé L (2008) Three-dimensional numerical characterization and modeling of natural fracture networks. Application to the reservoirs cases, PhD Thesis, National Polytechnic Institute of Lorraine, France (In French).

Mamtani MA, Vishnu CS, Basu A (2012) Quantification of microcrack anisotropy in quartzite-A comparison between experimentally undeformed and deformed samples, *Journal of the Geological Society of India* 80: 153-166.

Mandelbrot B (1967) How is the Coast of Britain? Statistical Self-similarity and Fractional Dimension, *Science* 156: 636-638.

Mandelbrot B (1982) The fractal geometry of nature, Freeman, San Francisco, USA.

Mandelbrot B (1985) Self-affine fractals and fractal dimension, *Physica Scripta* 32: 257-260.

Manjusha OT, Mukherjee S. (Submitted) Fuzzy graph theory applied to brittle plane network- A need for carbon sequestration models. *Journal of Geosciences Research*. https://doi.org/10.31223/X5B643

Mansouri H, Bafti A S, Poukermani M (2020) The power law scaling geometric and kinematic characteristic of faults in the Northern part of the Kerman Coal Province (KCP) Iran, Iranian *Journal of Earth Sciences* 112: 124-132.

Manzocchi T (2002) The connectivity of two-dimensional networks of spatially correlated fractures, *Water Resources Research* 38: 1-20.

Marwan N, Saparin P, Kurths J (2007) Measures of complexity for 3D image analysis of trabecular bone, *European Physical Journal-special Topics* 143: 1-9.

Mašín D (2003) Application of the fractal fragmentation model to the fill of natural shear zones. In: Fractals in Geotechnical Engineering. Editor: Kolymbas. Logos, Berlin: 57-65.

Matar S, Ghilardini L, Degroen V, Lemaux T, Singa Ray D, Al-shemali A (2010) Characterization Modelling and Simulation of the Fractured Najmah-Sargelu Carbonate Reservoir Umm Gudair Field West Kuwait, Society of Petroleum Engineers, 14th Abu

Dhabi International Petroleum Exhibition and Conference, Abu Dhabi, UAE.

Matsumoto N, Yomogida K, Honda S (1992) Fractal analysis of fault systems in Japan and the Philippines, *Geophysical research Letters* 19, 4: 357-360.

McGrath AG, Davison I (1995) Damage zone geometry around fault tips, *Journal of Structural Geology* 17: 1011-1024.

Mukherjee S. (2019) Using graph theory to represent brittle plane networks. In: Billi A, Fagereng A (Eds) Problems and Solutions in Structural Geology and Tectonics. Developments in Structural Geology and Tectonics Book Series. Vol. 5. Series Editor: Mukherjee S. Elsevier: 259-272. ISSN: 2542-9000.

Munz D, Fett T (2001) Ceramics-Mechanical Properties, Failure Behaviour, Materials Selection, Springer, Berlin.

National Research Council (1996) Committee on Fracture Characterization and Fluid Flow, Rock Fractures and Fluid Flow: Contemporary Understanding and Applications, National Academy Press, Washington DC, USA.

Nosjean N, Khamitov Y, Rodriguez S, Yahia-Cherif R (2020) Fracture corridor identification through 3D multifocusing to improve well deliverability an Algerian tight reservoir case study, *Solid Earth Sciences* 5: 31-49.

Odling NE, Gillespie P, Bourgine B, Castaing C, Chilès JP, Christensen NP, Fillion E, Genter A, Olsen C, Thrane L, Trice R, Aarseth E, Walsh JJ, Watterson J (1999) Variations in fracture system geometry and their implications for fluid flow in fractured hydrocarbon reservoirs, *Petroleum Geosciences* 5: 373-384.

Okubo PG, Aki K (1987) Fractal geometry in the San Andreas fault system, *Journal of Geophysical Research* 92: 345–355.

Ord A, Hobbs B (2019) Quantitative measures of deformed rocks: The link to dynamics, *Journal of Structural Geology* 15: 74-81.

Ouillon G, Castaing C, Sornette D (1996) Hierarchical geometry of faulting, *Journal of Geophysical Research* 101, B3: 5477-5487.

Paredes C, Elorza FJ (1999) Fractal and multifractal analysis of fractured geological media: surface-subsurface correlation, *Computers & Geosciences* 25: 1081-1096.

Park S-I, Kim Y-S, Ryoo C-R, Sanderson D J (2010) Fractal analysis of the evolution of a fracture network in a granite outcrop SE Korea, Geosciences *Journal* 14: 201-215.

Peacock DCP (2001) The temporal relationship between joints and faults, *Journal of Structural Geology* 23: 329-341.

Peacock DCP, Mann A 2005, Evaluation of the controls on fracturing in reservoir rocks, Journal of Petroleum Geology 28 (4) 385–396.

Peacock DCP, Sanderson DJ, Bastesen E, Rotevatn A, Storstein TH (2019) Causes of bias and uncertainty in fracture network analysis, *Norwegian Journal of Geology* 99: 1 1-15.

Peitgen H-O, Jürgens H, Saupe D (1992) Chaos and Fractals, New Frontiers of Science, Springer New York, USA.

Peng J, Haodong H, Xia Q, Li B (2018) Evaluation of the pore structure of tight sandstone reservoirs based on multifractal analysis: a case study from the Kepingtage Formation in the Shuntuoguole uplift Tarim Basin NW China, *Journal of Geophysics and Engineering* 15: 1122-1136.

Pérez-López R, Giner-Robles JL, Martínez-Díaz JJ, Rodríguez-Pascua MA, Bejar M, Paredes C, González-Casado JM (2007) Active tectonics on Deception Island (West-Antarctica): A new approach by using the fractal anisotropy of lineaments fault slip measurements and the caldera collapse shape, A Keystone in a Changing World-Online, Proceedings of the 10th International Symposium on Antarctic Earth Sciences, US Geological Survey and The National Academies Short Research, USA.

Pérez-López R, Parades C (2006) On measuring the fractal aisotropy of 2-D gemetrical sets : Application to spatial distribution of fractures, *Geoderma* 134: 402-414.

Pérez-López R, Paredes C, Muñoz-Martín A (2005) Relationship between the fractal dimension anisotropy of the spatial faults distribution and the paleostress fields on a Variscan granitic massif (Central Spain): the F-parameter, Journal *of Structural Geology* 27: 663-677.

Peron P, Guiraud M, Vennin E, Moretti I, Portier E, Le Pourhiet L, Konaté M (2018), Influence of basement heterogeneity on the architecture of low subsidence rate Paleozoic intracratonic basins (Reggane Ahnet Mouydir and Illizi basins Hoggar Massif), *Journal of Geophysical Research* 9: 1239-1275.

Peternell M, Kruhl JH (2009) Automation of pattern recognition and fractal-geometry-based pattern quantification exemplified by mineral-phase distribution patterns in igneous rocks *Computers & Geosciences* 35: 1415-1426.

Pickering G, Bull JM, Sanderson DJ (1995) Sampling power law distributions, *Tectonophysics* 248: 1-20.

Plotnick RE, Gardner RH, Hargrove WW, Prestegaard K, Perlmutter M (1996) Lacunarity analysis: A general technique for the analysis of spatial patterns, *Physical Review* E 53: 5461-5468.

Plotnick RE, Gardner RH, O'Neill RV (1993) Lacunarity indices as measures of landscape texture, *Landscape Ecology* 8: 201–211.

Pohn NA (1981) Joint spacing as a method of locating faults, *Geology* 9: 258–261.

Putot C, Chastanet J, Cacas MC, Daniel JM (2001) Fracturation naturelle d'un massif rocheux : diaclases et couloirs de fracturation, *Oil & Gaz Science*

Technology, Revue de l'Institut Français du Pétrole 56: 431–449 (In French).

Rasband SW (1997) Image J, Open source image processing, National Institutes of Health and the Laboratory for Optical and Computational Instrumentation, University of Wisconsin), https://imagej,net/Download.

Riley P, Tikoff B, Murray AB (2011) Quantification of fracture networks in non-layered massive rock using synthetic and natural data sets, *Tectonophysics* 505: 44-56.

Rives T, Razack M, Petit JP, Rawsley KD (1992) Joint spacing: analogue and numerical simulations, *Journal of Structural Geology* 14: 925–937.

Roduit N (2010) JMicroVision: Image analysis toolbox for measuring and quantifying components of high-definition images, Version 1, 2, 7.

Roy A (2006) A quantitative study of scaling properties of fracture networks, MSc thesis University of Tennessee, USA.

Roy A (2013) Scale-dependent heterogeneity in fracture data sets and grayscale images, PhD thesis, The University of Tennessee, Knoxville, USA.

Roy A, Perfect E, Dunne WM, McKay LD (2007) Fractal characterization of fracture networks: An improved box-counting technique, Journal *of Geophysical Research* 112: 1-11.

Sahu AK, Roy A (2020) Clustering Connectivity and Flow Responses of Deterministic Fractal-Fracture Networks, *Advances in Geosciences* 54: 149-15.

Sanderson D, Nixon CW (2015) The use of topology in fracture network characterization, *Journal of Structural Geology* 72: 55–66.

Sanderson DJ, Peacock DCP, Nixon CW, Rotevatn A (2019) Graph theory and the analysis of fracture networks, *Journal of Structural Geology* 125: 155-165.

Sanderson JD, Peacock DCP (2019) Line sampling of fracture swarms and corridors, *Journal of Structural Geology* 122: 27-37.

Saucier A, Muller J (1999) Textural analysis of disordered materials with multifractals, *Physica* A1: 221-238.

Scholz CH (2002) The Mechanics of Earthquakes and Faulting, Cambridge University Press Cambridge, UK.

Segall P, Pollard D (1983) Joint formation in granitic rock of the Sierra Nevada, *Geological Society of America Bulletin* 94: 563–575.

Sharland PR, Archer R, Casey DM, Davies RB, Hall SH, Heward AP, Horbury AD, Simmons MD (2001) Arabian plate sequence stratigraphy, *GeoArabia, Special Publication* 2: 1–371.

Silva JP, Gomees IF, Santos RFVC, Miranda TSD, Guedes RP, Barbosa JA, Guimarães EX, Bessera LB, Guimarães LJDN (2021) Topological analysis of fracture networks integrated with flow simulation models for equivalent fracture permeability estimation, *Journal of Structural Geology* 147: 104338.

Soliva R, Benidicto A, Maerten L (2006) Spacing and linkage of confined normal faults: importance of mechanical thickness, *Journal of Geophysical Research* 111: 1–17.

Sornette A, Davy P, Sornette D (1993) Fault growth in brittle-ductile experiments and the mechanics of continental collisions, *Journal of Geophysical Research* 98: 111–139.

Spyropoulos C, Griffth WJ, Scholz CH, Shaw BE (1999) Experimental evidence for different strain regimes of crack populations in a clay model, *Geophysical Research Letters* 26: 1081-1084.

Stoyan D, Gloaguen R (2011) Nucleation and growth of geological faults, *Nonlinear Processes in Geophysics* 18: 529-536.

Stoyan D, Stoyan H (1994) Fractals Random Shapes and Point Fields, Methods of Geometrical Statistics, John Wiley and Sons, USA.

Tanaka M, Kayama A, Kato R, Ito Y (1999) Estimation of the fractal dimension of fracture surface patterns by Box-counting method, *Fractals* 7: 335-340.

Tchalenko JS, Ambraseys NN (1970) Structurale analyses of the Dasht-e-Bayaz (Iran) earthquake fractures, *Geological Society of America Bulletin* 81: 41–60.

Tran NH, Valencia K, Tran K, Rahman SS (2006) Hybrid Modelling using Neuro Fractal for Fractured Reservoirs, Proceeding of the5th WSEAS International Conference on Applied Computer Science, Hangzhou, China.

Turcotte DL (1989) Fractals in Geology and Geophysics, *Pure and Applied Geophysics* 131: 171–196.

Turcotte DL (1992) Fractals and Chaos in Geology and Geophysics, Cambridge University Press Cambridge, UK.

Vasilyev S (2016) Curve Fitting Software FindGraph (Version 2,49), Pacific Business Centre Vancouver Canada www,uniphiz,com.

Velandia F, Bermúdez MA (2018) The transpressive southern termination of the Bucaramanga fault (Colombia): Insights from geological mapping stress tensors and fractal analysis. *Journal of Structural Geology* 115: 190-207.

Velde B, Dubois J, Touchard G, Badri A (1990) Fractal analysis of fractures in rocks: the Cantor's Dust method, Tectonophysics 179: 345-352.

Vignes-Adler M, Le Page A, Adler PM (1991) Fractal analysis of fracturing in two African regions, from satellite imagery to ground scale, T*ectonophysics* 196: 69–86.

Villemin T, Sunwoo C (1987) Distribution logarithmique self-similaire des rejets et longueurs des failles: exemple du Bassin houiller Lorrain. *Comptes Rendus de l'Académie des Sciences, Paris* 305: 1309-1312 (in French).

Volland S, Kruhl JH (2004) Anisotropy quantification: the application of fractal geometry methods on tectonic fracture patterns of a Hercynian fault zone in NW-Sardinia, *Journal of Structural Geology* 26: 1489-1500.

Weibull W (1951) A Statistical Distribution Function of Wide Applicability. *Journal of applied Mechanics* 18 (3): 293-297.

Wheeler RL, Dixon JM (1980) Intensity of systematic joints: methods and application, *Geology* 8: 230–233.

Wu H, Sun Y, Shi W, Chen X, Fu D (2013) Examining the Satellite-Detected Urban Land Use Spatial Patterns Using Multidimensional Fractal Dimension Indices, *Remote Sensing* 5: 5152-5172.

Wu S, Groshong JrRH (1991) Low temperature deformation of sandstone southern Appalachian fold-thrust belt, *Geological Society American Bulletin* 103: 861–875.

Xie S, Cheng Q, Ling Q, Li B, Bao Z, Fan P (2010) Fractal and multifractal analysis of carbonate pore-scale digital images of petroleum reservoirs, *Marine and Petroleum Geology* 27: 476-485.

Zazoun RS (2001) (Hercynian deformation in the western Ahnet Basin and Bled El-Mass area, Algerian Sahara: a continuous strain, *Journal of African Earth Sciences* 32: 869–887 (in French).

Zazoun RS (2008) The Fadnoun area Tassili-n-Azdjer Algeria: fracture network geometry analysis, *Journal of African Earth Sciences* 50: 273–285.

Zazoun RS, Marok A, Samar L, Bebadla M, Mezlah H (2015) Fracturing and deformation bands in the El Kohol area (Central Saharan Atlas Algeria): fractal analysis scaling laws and discrete fracture network modelling, *Estudios Geológicos* 71: 1-23 (In French).

Zieliński M (2011) Reconstruction of thermal history of the Ahnet and Mouydir basins (southern Algeria), PhD thesis Institute of Geology Faculty of Geographical and Geological Sciences Adam Mickiewicz University Poznan, Poland.

Zimmerman R, Main I (2004) Hydromechanical behavior of fractured rocks, *International Geophysics Series* 89: 363-422.